Chem Soc Rev

Silica-based nanoparticles: a versatile tool for the development of efficient imaging agents

Journal:	*Chemical Society Reviews*
Manuscript ID:	CS-REV-08-2014-000270.R1
Article Type:	Review Article
Date Submitted by the Author:	07-Aug-2014
Complete List of Authors:	Caltagirone, Claudia; Università degli Studi di Cagliari, Dipartimento di Scienze Chimiche e Geologiche Bettoschi, Alexandre; Universita' degli Studi di Cagliari, Dipartimento di Scienze Chimiche e Geologiche; Università degli Studi di Cagliari, Dipartimento di Scienze Chimiche e Geologiche Garau, Alessandra; Università degli Studi di Cagliari, Dipartimento di Scienze Chimiche e Geologiche Montis, Riccardo; Universita' degli Studi di Cagliari, Dipartimento di Scienze Chimiche e Geologiche; Università degli Studi di Cagliari, Dipartimento di Scienze Chimiche e Geologiche

Journal Name

RSCPublishing

ARTICLE

Silica-based nanoparticles: a versatile tool for the development of efficient imaging agents

Cite this: DOI: 10.1039/x0xx00000x

Claudia Caltagirone,* Alexandre Bettoschi, Alessandra Garau and Riccardo Montis

Received ooth January 2012,
Accepted ooth January 2012

DOI: 10.1039/x0xx00000x

www.rsc.org/

This review describes the recent advances in the development of imaging agents based on silica nanoparticles. Different techniques (magnetic resonance imaging, optical imaging, positron emission tomography, X-ray computed tomography, and ultrasound imaging) are described as well as the possibility of combining together in the same nanoplatform different imaging techniques and simultaneously perform imaging and therapy.

Introduction

Early diagnosis and effective treatment of the diseases are the main goals of nanomedicine, a recent and highly active multidisciplinary research field that combine together chemistry, biology, pharmaceutics and medicine with the help of the nanotechnologies.[1] For this reason non-invasive bioimaging techniques, being a powerful tool for the diagnosis of various diseases, has rapidly improved with the development of nanomaterials as contrast agents (CAs) and molecular probes.[2-4] Traditional CAs such as organic dyes or radioisotopes conjugated with targeting ligands are currently used in both research and clinical practice,[5] however, inorganic nanoparticles (INPs) are receiving increasing attention as CAs because of their peculiar features such as high thermal/chemical stability and resistance to corrosion in physiological conditions. INPs such as semiconductor quantum dots (QDs),[6-8] metallic NPs[9, 10] or magnetic NPs[11, 12] have found applications in nanomedicine.[13]

Among INPs, silica nanoparticles are one of the most biocompatible being endogenous for most living organisms. Moreover, they are "Generally Recognised As Safe" (GRAS) by the U.S. Food and Drug Administration (FDA),[14] although investigations are in due course to completely exclude the possible hazards deriving from their small dimensions.[15] Silica NPs offer numerous advantages over other INPs, such as well-defined and tunable structures in terms of size, morphology and porosity. They can be easily prepared from inexpensive starting materials and functionalised by well-established siloxane chemistry or loaded with therapeutics or CAs, so that new properties can be imparted to the material. The internalisation into the nanostructure grants the loaded species increased chemical stability, a protection from enzymatic degradation and an almost constant chemical environment.[16, 17] Moreover, silica NPs are transparent in the ultraviolet, visible and near infrared (NIR) regions of the electromagnetic spectrum and they do not interfere with the magnetic radiation. For all these reasons they are ideal candidates for the development of new and efficient diagnostic and therapeutic agents. Indeed, the fluorescent silica NPs, known as "Cornell Dots" have been approved by FDA for the first in human clinical trial as imaging agent for a model human melanoma in January 2011.[18]

There are two major classes of silica-based nanoparticles, solid (SiNPs) and mesoporous (MSNs). The former are normally obtained using three main synthetic approaches: the Stöber-Van Blaaderen,[19] reverse microemulsions (water in oil)[20] or direct micelles assisted methods.[21] SiNPs have been extensively used as optical imaging agents. On the other hand, MSNs are normally synthesised by a surfactant-templated sol-gel method[4, 22] and they are characterised by high surface areas, stable and rigid frameworks, tunable pore sizes and large pore volumes in which functional molecules (CAs and/or drugs) can be encapsulated and sheltered from the environment. Moreover, silica can be used as shell for metallic NPs.

In this review various recent examples of SiNPs, and MSNs for bioimaging applications, mostly *in vivo*, will be described. The majority of the chosen examples refer to tumour imaging and throughout the review the importance of NPs targeting will be pointed out. Indeed well-designed nanoparticles with an

optimal size can have passive enhanced permeability and retention (EPR) effects to accumulate in tumour tissue due to the imperfect angiogenesis of tumours' blood vessels.[23-27] When the NPs are functionalised with aptamers, peptides or specific receptors that allow their selective accumulation in well-defined tissues or cells we refer to targeted NPs and in this case the cellular uptake depends on an active mechanism.

Different type of bioimaging techniques are available and each have advantages and disadvantages in terms of resolution, depth of penetration into organs, sensitivity, and financial cost.[28] Indeed imaging techniques are complementary rather than competitive[28] and a selection of vey recent examples (2013-2014) of multimodal systems will be described.

Finally, a section will be dedicated to the most relevant recent examples of silica-based NPs for bioimaging and therapy as scientists are putting much effort to obtain efficient systems able to simultaneously perform diagnosis and to cure the diseases

Magnetic Resonance Imaging (MRI)

Magnetic Resonance Imaging (MRI) is one of the most powerful diagnostic tool for clinical imaging thanks to its exceptional spatial and anatomical resolution, routinely down to 0.5-1mm.[29, 30] The MRI signal is generated by the relaxation of the protons of water molecules, located in different physiological environment, in the presence of a magnetic field. The differences in the relaxation times, both longitudinal (T_1) and transverse (T_2), mostly depend on the type of tissue in which the protons are located and they are used to generate images. Paramagnetic metal ions (Gd^{3+} and Mn^{2+}, in particular) are able to decrease both T_1 and T_2 thus acting as catalysts for the returning in the ground state of the protons, improving in this way the image contrast.[31-42] Although MRI is one of the most important imaging tool in medical diagnostic, this technique has a major drawback represented by its low sensitivity.[43] Indeed, a relatively large local concentration of contrast agents is required (about 10^{-5} M) in order to achieve a contrast enhancement.[44] In order to increase the sensitivity of the technique, the classic contrast agents can be incorporated into nanoparticles so that a larger number of paramagnetic metal ions can be delivered to the site of interest increasing the quality of the imaging.[45] Mesoporous silica nanoparticles (MSNs) are an ideal platform for the development of MR-enhancing materials. Lin and coworkers have coated MSNs with a Gd-Si-DTTA (diethylenetriamine tetraacetic acid) complex, as schematically shown in Figure 1a to obtain high efficient MRI contrast agents, with a pore diameter of 0.9-1.0 nm.[46]

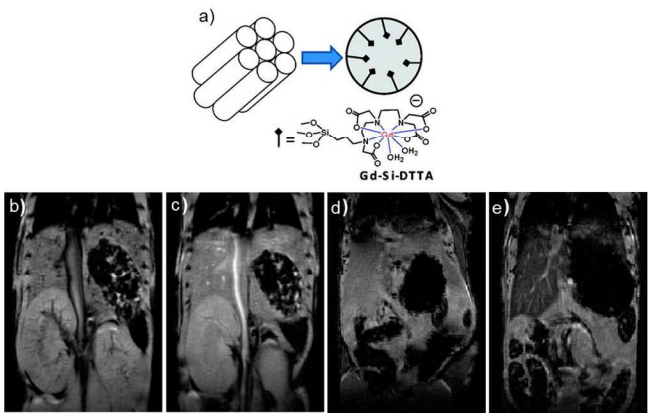

Figure 1 a) Schematic representation of the Gd-Si-DTTA complexes in the hexagonally ordered nanochannels of the MSNs. b) Pre-contrast and c) post-contrast T_1-weighted mouse MR image showing aorta signal enhancement. d) Pre-contrast and e) post-contrast T_2-weighted mouse MR image showing liver signal loss. Adapted with permission from JACS, 2008, 130, 2154-2155. Copyright 2008 ACS.

A very large longitudinal and transverse relaxivity (often the relaxivity r_1 and r_2 ($1/T_1$ and $1/T_2$, respectively) are taken into account to describe the efficiency of a contrast agent) was observed ($7.0 \cdot 10^5$ $mM^{-1}s^{-1}$ and $1.6 \cdot 10^6$ $mM^{-1}s^{-1}$ at 3.0 T, respectively, and $2.48 \cdot 10^5$ $mM^{-1}s^{-1}$ and $2.7 \cdot 10^6$ $mM^{-1}s^{-1}$ at 9.4 T, respectively on a per millimolar particles basis). The observed values were much larger than those observed for solid silica nanoparticles ($2.0 \cdot 10^5$ $mM^{-1}s^{-1}$ and $6.1 \cdot 10^5$ $mM^{-1}s^{-1}$ at 3.0 T, respectively on a per millimolar particles basis) coated with a Gd-DTPA (diethylene triamine pentaacetic acid) derivative previously reported by the same research group.[47] This difference in the relaxivity could be attributed to the different nature of the Gd^{3+} complex. The 3-(4,5-dimethylthiazol-2-yl)-5-(3-carboxymethoxyphenyl)-2-(4-sulfophenyl)-2H-tetrazolium (MTS) viability cells assay demonstrated that the nanoparticles were non-toxic for monocyte cells after incubation with 10 µg of nanoparticles per 5000 cells after 26h, and a viability of 85% was observed after incubation with 100 µg of nanoparticles per 5000 cells after the same period of time.

The effectiveness of the MSNs-Gd as *in vivo* MR contrast agent was evaluated by injection of 2.1 µmol/kg body in a DBA/1J mouse upon tail vein using a 9.4 T scanner. As shown in Figure 1b and 1c after 15 minutes form injection a T_1-weighted enhancement was clearly visible in the aorta of the mouse. When a higher dosage of MSN-Gd was injected (31 µmol/kg body) a liver signal loss was also observed (Figures 1d and 1e) after 1h from injection, depending on a T_2-weighted enhancement. This was attributed to the phagocytosis of the MSN-Gd by the liver macrophages cells.

Huang and co-workers have also synthesized MSNs conjugated with both fluorescein isothiocyanate (FITC) and DTPA as the chelating agent for Gd^{3+}, obtaining nanoparticles with spherical morphology of about 100 nm.[48] MRI using a clinical 1.5 T MR scanning both *in vitro* on hMSCs (Human Mesenchymal Stem Cells) and *in vivo* (on a mouse) was performed. In particular,

authors reported that the NPs are non- toxic, do not affect cell viability, growth or differentiation of hMSCs. Moreover, the NPs were labelled with hMSCs and implanted into the basal ganglions of a nude mouse. As shown in Figure 2, the coronal plane of T_1-weighted images revealed a bright dot which could be observed for at least 14 days. This result demonstrated that no migration of hMSCs occurred and that the proposed NPs could be used to track stem cells.

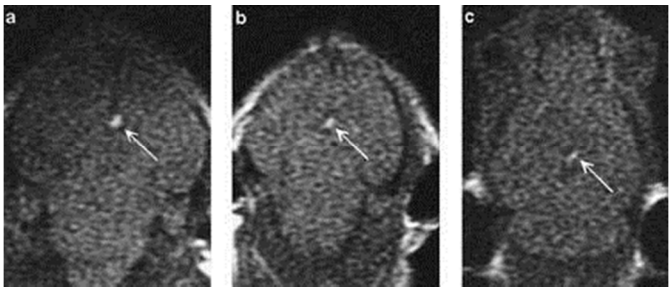

Figure 2 MRI of hMSCs injected to the midline high brain stem of a nude mouse after 0 days (a), 7 days (b) and 14 days (c) from the injection. Images were collected using a 1.5-T MR scanning. Reproduced with permission from Small, 2008, 4, 1445-1452. Copyright 2008 Wiley-VCH.

Other examples of MSNs functionalised with Gd^{3+} complexes have been recently reported by Mazzanti,[49] Botta and Marchese,[50] and Mayer.[51] All the synthesised materials showed a remarkable enhancement of relaxivity, however no MRI imaging have been reported so far.

Rocha and collaborators prepared mixed lanthanide-DTPA silica nanoparticles in which Gd^{3+} (for MRI) and Eu^{3+} or Tb^{3+} (for optical imaging) were grafted on the NPs to obtain the hybrid system SiO_2@APS/DTPA:Gd:Ln (APS = 3-aminopropyltrimetoxysilane, Ln = Eu^{3+} or Tb^{3+}).[52] This study took inspiration from other multimodal probes in which core-shell hybrid nanoporous sililica NPs containing a luminescent $[Ru(bpy)_3]Cl_2$ core (bpy = 2,2′bypyridine) and a paramagnetic monolayer coating of a silylated Gd^{3+} complex were studied.[47, 53, 54] Authors demonstrated that the incorporation of Gd^{3+} in the nanosystem did not change the emission properties of the luminescent Eu^{3+} and Tb^{3+}, and that the relaxometric features of the system were slightly better than those of the commercially available $[Gd(DTPA)]^{2-}$. The nanoparticles were rapidly and efficiently uptake by RAW 264-7 cells (mouse macrophage cell line) and showed an enhancement of the T_1-weighted MRI measured on a 3.0 T scanner, as shown in Figure 3 (III), compared to unexposed cells (I) and opposite to the strong negative contrast due to the T_2-shortening Fe_2O_3 NPs (II).

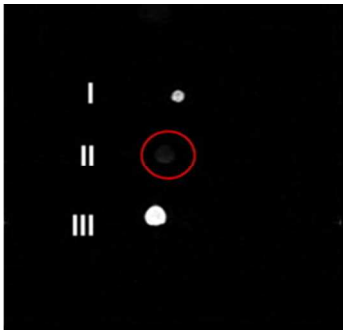

Figure 3 T_1-weighted MRI of cellular pellets of no NPs internalisation (I), γ-Fe_2O_3 NPs (II) and SiO_2@APS/DTPA:Gd:Eu NPs (III). Adapted with permission from Biomaterials, 2012, 33, 925-935. Copyright 2012 Elsevier Ltd.

More recently the same group reported on the hybrid system SiO_2@APS/PMN:Gd:Eu (PMN = 2,2′,2″,2‴-[(Pyridine-2,6-diyl)bismethylenenitrilo]-tetrakis(acetic acid).[55] An increase in the T_1-weighted MRI in the RAW 264-7 cells is observed compared to the SiO_2@APS/PMN:Gd.

Although the strategy of incorporating Gd^{3+} complexes has been extensively used, it presents some major drawbacks such as the possibility that, even if Gd^{3+} is chelated by organic ligands, during the metabolic process the release of the metal ion *in vivo* can still occur.[56] For this reason, novel nanoparticles for MRI have been developed, containing Gd^{3+} as Gd_2O_3 coated by mesoporous SiO_2. Li and co-workers have reported on a novel one step synthesis for this purpose obtaining nanoparticles with a uniform size distribution and an average size of 20-40 nm.[57] An increase of T_1 *in vitro* was observed for Gd_2O_3@SiO_2 compared to that of Gd-DTPA. Gd_2O_3@SiO_2 were also evaluated as *in vivo* MRI contrast agents by injecting through the tail vein of a mouse 100 µL saline solution containing 100 mg/mL Gd nanoparticles. As shown in Figure 4a after 15 minutes from the injection the nanoparticles were mainly concentrated in the liver. After 30 minutes from injection an increase in the signal of a xenografted tumour was observed (Figure 4b), demonstrating that the nanoparticles had the right size to penetrate neoplastic vascular endothelial gaps and could concentrate in tumour tissues. MRI intensity enhancement lasted more than 24 h indicating a slow renal metabolization of the contrast agent. The same authors have also demonstrated *via* DFT calculations that in Gd_2O_3@MCM-41 Gd^{3+} ions could not be dissociated from silica. Moreover, it was shown that the nanocomposite were non-toxic and accumulated preferentially in liver, spleen, and lungs, than in kidneys, heart and brain.[58]

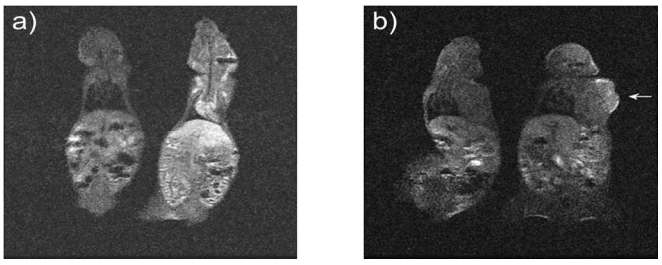

Figure 4 a) control (left) and post-contrast (right) T_1-weighted MR images depicting signal enhancement in mouse liver; b) control (left) and post-contrast (right) T_1-weighted MR images displaying signal enhancement in xenografted tumour (white arrow). Adapted with permission from Contrast Media Mol. Imaging, 2011, 6, 110-118. Copyright 2011 Wiley-WCH.

As described above, the chelates complexes of Gd^{3+} and the nanoparticles containing this metal ion are able to enhance the r_1 contrast. On the other hand, it is well known that magnetite nanoparticles (Fe_3O_4) can find application in many biomedical fields. However, concerning their application as MRI contrast agents, they have a limited effect on r_2 relaxivity. For this reason Yeh and co-workers have recently synthesized Gd^{3+} chelated Fe_3O_4@SiO_2 using DOTA (1,4,7,10-tetraazacyclododecane-1,4,7,10-tetraacetic acid) as a chelator for the metal ion.[59] The presence of the Gd^{3+} ions within the silica shell causes an increase of r_2 from 97 $mM^{-1}s^{-1}$ of Fe_3O_4 to 681 $mM^{-1}s^{-1}$ for the Gd^{3+}-chelated Fe_3O_4@SiO_2. In order to study the possible *in vivo* application of the new nanoparticles rats were treated with the Gd^{3+}-chelated Fe_3O_4@SiO_2 (0.5 mg/kg) and then MR images were acquired at different times using a 3.0 T scanner and a 7.0 T animal micro-MRI system. As shown in Figure 5 for the T_2-weighted imaging, the imaging contrast of the lymph nodes (white arrows), liver (red arrows), spleen (blue arrows), and kidneys (orange arrows) was darkened after injection. Moreover, the Gd^{3+}-chelated Fe_3O_4@SiO_2 nanoparticles shown a certain tendency to accumulate in the lymph nodes compared to iron oxide nanoparticles which accumulate only in the normal nodes. This result is quite interesting because of the central role of the lymph nodes during tumour diagnosis, staging and clinical treatment.

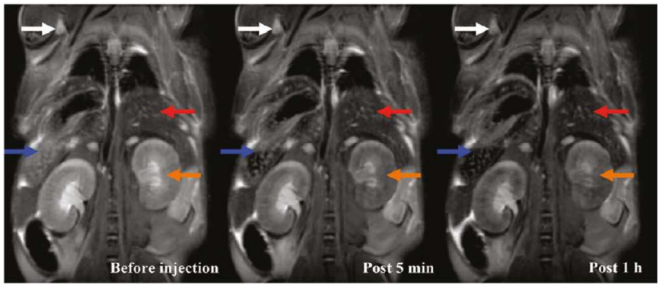

Figure 5 *In vivo* micro-T_2-weighted imaging of mice at pre-injection, 5 minutes, and 1 hour postinjection using a 7.0 T animal micro-MRI system. White arrows, lymph nodes, red arrows, liver, blue arrows, spleen, and orange arrows, kidneys. Adapted with permission from ACS Nano, 2011, 5, 3905-3916. Copyright 2011 ACS.

Numerous examples of magnetic nanoparticles as MRI contrast agents have been reported in the literature. In particular, the so-called SPIONs featuring a Fe_3O_4 core with a superparamagnetic behaviour which is a desirable property for T_2 MRI contrast agents.[60]

Mou and co-workers have developed a strategy to combine amorphous silica shells of Fe_3O_4@SiO_2 with MSNs functionalized with a fluorophore (fluorescein isothiocyanate, in particular) and they reported the first example of direct injection of MSNs in mice *in vivo* and their localization *via* MRI.[61] The nanoparticles (named Mag-Dye@MSNs) were administered through eye vein injection (5 mg Fe per kg of mouse body weight) and the *in vivo* contrast enhancing effect was measured with a 7.0 T MRI system. As shown in Figure 6 after injection the nanoparticles tend to accumulate more in liver and spleen than in kidneys. Indeed after 120 minutes they were cleared from the kidneys.

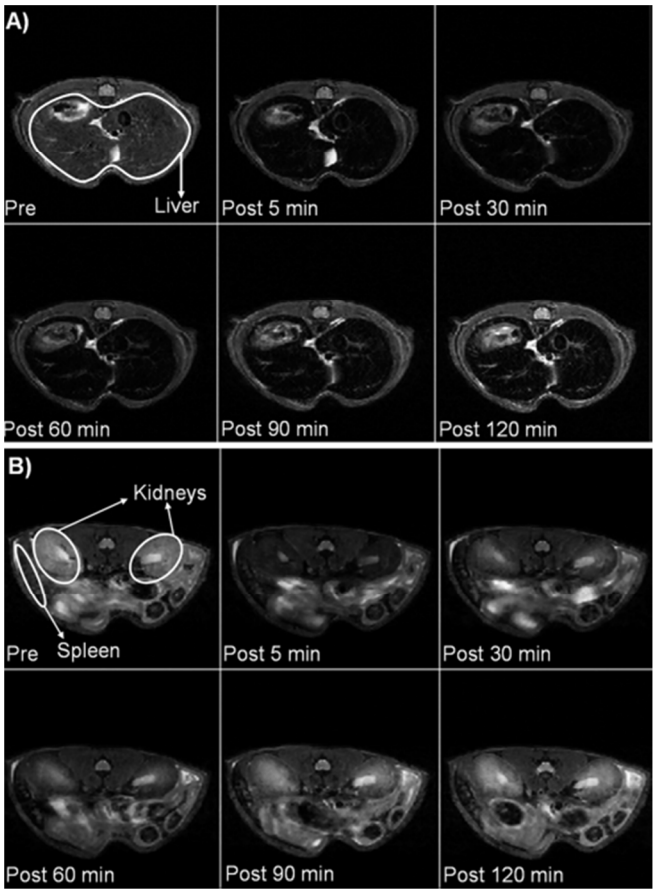

Figure 6 *In vivo* T_2-weighted MR images showing time-dependent darkening in MR images of A) Liver, and B) kidneys/spleen before and after (5, 30, 60, 90, and 120 min) administration of 5 mg Fe per kg body weight of Mag-Dye@MSNs. Reproduced with permission from ChemBioChem, 2008, 9, 53-57. Copyright 2008 Wiley-WCH.

The same nanoparticles have demonstrated to be internalised in NIH 3T3 fibroblast cells[62] and were used to label hMSCs and then imaged them.[63] Authors firstly determined the minimum detectable number of hMSCs (around $1.2 \cdot 10^4$ to $3 \cdot 10^4$), using a 1.5 T MRI, by incubating the cells with 30 μg mL Mag-Dye@MSNs for 1 hour. Then the MRI of hMSCs labelled with Mag-Dye@MSNs in a nude mice model was performed. As shown in Figure 7a a dark signal at the frontal cortex of the mouse brain could be observed 8h after implantation.

Figure 7 MR images of nude mouse after 8 h (a) and 9 days (b) after implantation of Mag-Dye@MSNs-labelled hMSCs at the frontal cortex. The stem cells are visualised as a dark dot (white arrow). Reproduced with permission from *Small*, 2008, 4, 619-626. Copyright 2008 Wiley-WCH.

After 9 days the stem cells could still be visualised (Figure 7b). With the aim of render the nanoparticles more biocompatible preventing the non-specific adsorption of proteins, Hyeon, Moon and co-workers modified the surface of Fe_3O_4@MSNs with PEG (polyethylene glycol) and incorporated fluorescein isothiocyanate or rhodamine B isothiocyanate and described the first example of accumulation of MSn intravenously injected on a tumour site.[64] The NPs, having a Fe_3O_4 core of 15 nm, showed a r_1 and r_2 relaxivity values of 3.40 and 254 $mM^{-1}s^{-1}$. The passive tumour accumulation *via* EPR of the NPs was monitored by injecting them into nude mice bearing a tumour on their shoulder. As shown in Figure 8 after 2h from the injection the accumulation of the NPs in the tumour could be detected by NMR (white arrows) and the tumour could still be visualised after 24h.

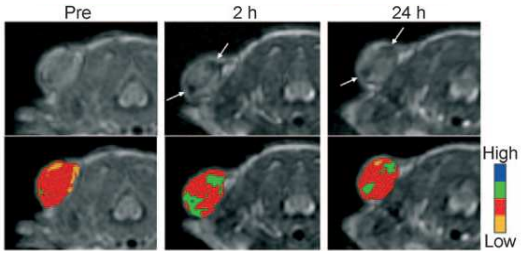

Figure 8 *In vivo* T_2 weighted MR images (upper row) and colour maps (lower row) of T_2 weighted MR images of tumour in a nude mouse implanted with MCF-7 breast tumour cells before and after the injection of Fe_3O_4@MSNs-PEG incorporating the rhodamine derivative. Adapted with permission from *Angew. Chem. Int. Ed.*, 2008, 47, 8438-8441. Copyright 2008 Wiley-WCH.

In order to specifically target cancer cells, instead of exploiting the EPR mechanism, Shi and co-workers have recently synthesised rattle-type magnetic mesoporous silica nanoparticles (RMMSNs) whose surface was modified with PEG and cancer cell specific ligand folic acid (FA).[65] The nanoparticles were obtained by encapsulating Fe_2O_3 particles within mesoporous silica shells by selectively etching the middle silica interlayer. The specificity of the targeted NPs was tested on cells overexpressing folate receptor (HeLa cells) and not overexpressing the folate receptor as a negative control (MCF-7 cells). An effective increased uptake efficiency was observed in the case of the HeLa cells as demonstrated by the MR imaging of the cells performed on a clinical 3.0 T MR imaging scanner. A significant negative contrast enhancement was observed in the case of HeLA cells incubated with RMMSN-PEG-FA in comparison to MCF-7 cells.

Recently, Zhang and co-workers have demonstrated that fluorescent (FITC) mesoporous silica-coated SPIONs are able to track neural progenitor cells (C17.2).[66] The NPs showed a relaxivity r_2 of 309.53 $mM^{-1}s^{-1}$ and high efficiency for C17.2 cell labelling. For this reason the NPs labelled cells were intracerebrally injected in middle cerebral artery occlusion (MCAO) mice and could be tracked using a 3 T clinical MRI scanner. As shown in Figure 9a after 1 day from injection the hyperintense signal in the ischemic area diminished and after 3 days the hypointense signal at the ischemic site could be clearly observe. On the other hand, when the NPs labelled cells were intravenously injected (Figure 9b) the MR intensity of the ischemic area decreased, suggesting the accumulation of the NPs in the lesion site. After 3 days the signal intensity decrease was even more visible.

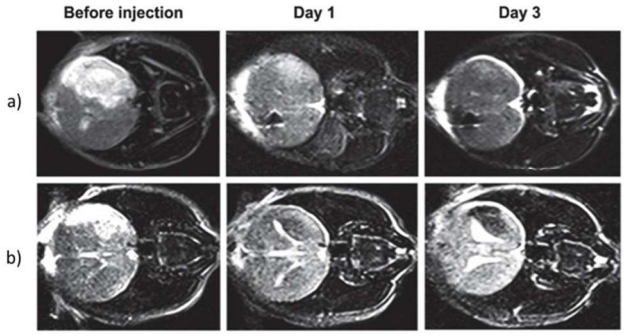

Figure 9 MRI tracking of Zhang's NPs labelled C17.2 cells infused intracerebrally (a) or intravenously (b) in MCAO mouse brain. Adapted with permission from Nanoscale, 2013, 5, 4506-4516. Copyright 2013 RSC.

From the examples reported above it is clear that when using SPIONs the MRI signal results in a hypointense region which cannot be distinguished from other hypointense regions such as haemorrhage or blood clots. For this reason a contrast agent that causes a positive contrast (as the Gd^{3+} containing CA described above) it would be auspicable. Manganese containing contrast agents are good candidate for this purpose being this element less toxic than gadolinium, and a few examples of MnO nanoparticles have been reported in the literature.[67, 68] In particular, Hyeon, Gillad and collaborators have developed mesoporous silica-coated hollow manganese oxide ($HMnO@mSiO_2$) which showed an enhancement in the r_1 value compared to other Mn-containing NPs.[69] $HMnO@mSiO_2$ were used to follow the fate of transplanted, labelled MCCs in mice with a clinical 9.4 T MRI scanner. As clearly shown in Figure 10 a hyperintense region was observed in the transplantation site (green arrows) and the NPs could be still visualized after 14 days.

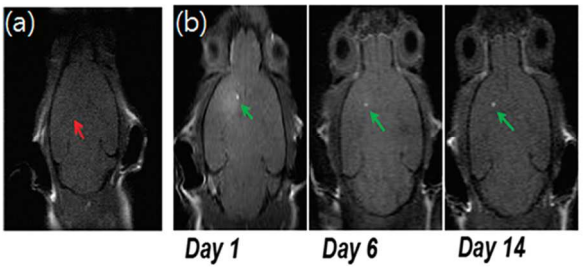

Figure 10 *In vivo* MRI of transplanted MSCs; a) unlabelled MSCs, b) hyperintense signal (green arrow) detectable in mouse transplanted with HMnO@mSiO$_2$ still visible after 14 days. Reproduced with permission from J. *Am. Chem. Soc.*, 2011, **133**, 2955-2961. Copyright 2011 ACS.

Fang, Yang and co-workers have recently proposed a new type of targeted core-shell nanoprobes named MnO_3@SiO_2(RB)-PEG-Apt for targeted T_1-MRI of small animal tumour xenografts.[70] They consisted on a hydrophobic core of MnO_3 encapsulated within an amino functionalised silica shell. The NPs contained also a fluorophore (rhodamine, RB) doped into the silica shell. The silica surface was modified with PEG in order to improve the biocompatibility of the system and then an aptamer (AS411) was conjugated on the terminal parts of the PEG chains as a targeting agent. The targeting effect of the NPs was evaluated *in vitro* using HeLa cells and then *in vivo* on a mouse model with an inoculated tumour. T_1-weighted MR images were obtained after injecting intravenously MnO_3@SiO_2(RB)-PEG-Apt to the animal using a clinical 1.5 T MR imaging system. As shown in Figure 11 after 0.5h and 1h from the injection the T_1-weighted MR images showed only a slight enhancement compared to the images of the non-injected tumour probably because in this period of time only a limited amount of NPs had reached the tumour site. After 12h the signal in the tumour showed a significant enhancement, while after 24h the signal enhancement decreased, suggesting a biodegradation or a clearance of the nanoparticles from the mouse body.

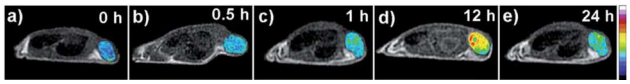

Figure 11 T_1-weighted MR images of a tumour-bearing mice model injected with MnO_3@SiO_2(RB)-PEG-Apt at different times a) 0h, b) 0.5h, c) 1h, d) 12h, e) 24h. The colour bar changing from black to white indicates the gradual increase in the MR intensity signal. Adapted with permission form Nanoscale 2013, 5, 10447-10454. Copyright 2013 RSC.

Recently Lee and co-workers have described Mn-SiO_2 nanoparticles obtained doping amorphous silica nanoparticles with Mn^{2+} and coating them with PEG, as a liver-specific MRI contrast agent.[71] In this case the T_1 enhancement was due to the release of Mn^{2+} ions only at acidic pH. At neutral pH, probably because water molecules were inaccessible for Mn^{2+} ions inside the silica, negligible relaxivity values were observed; in a citrate buffered solution at pH 5.0 the r_1 and r_2, measured with a 3.0 T human clinical scanner were found to be 6.7 $mM^{-1}s^{-1}$ and 23.3 $mM^{-1}s^{-1}$, respectively, similar to those observed for a citrate solution containing $MnCl_2$. This enhancement was attributed to the release of Mn^{2+} ions in acid solution. Mn-SiO_2 NPs were injected in hepatocellular carcinoma (HCC) model animals in order to validate their use for *in vivo* liver MR imaging. As shown in Figure 12, a gradual enhancement in the contrast of the parenchyma tissue was observed in the first 6h after the injection. On the other hand in the first 6h the signal intensity of the HCC tissues was hypointense, resulting in an overall enhanced contrast resolution between HCC tissues and normal liver tissue. This was attributed to the affinity of Mn-SiO_2 NPs for Kupfer cells which are located in the parenchyma of the liver (and not in the HCC tissue) and their activation by the acidic pH of the endosomal environment. At long time exposition (24-48h) the T_1-weighted signal intensity of parenchyma tissue decreased while the HCC signal become hyperintense due to the release of free Mn^{2+} from the Kupfer cells.

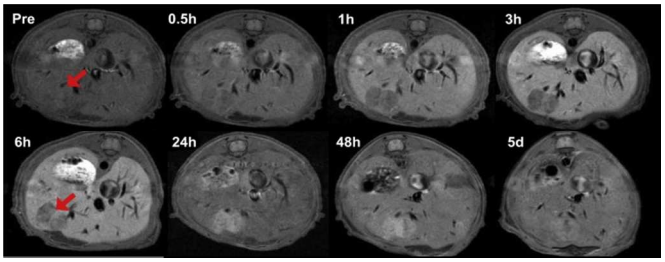

Figure 12 T_1-weighted MR image of a nude mouse liver from HCC (red arrow) before and after injection of Mn-SiO_2 NPs. Reproduced with permission from Biomaterials, 2013, 34, 8941-8948. Copyright 2013 Elsevier.

A particularly useful technique for monitoring biological samples is ^{19}F MRI because of the negligible effect of background signal.[72, 73] However, in order to obtain signals of adequate intensity it is necessary to increase the number of fluorine atoms in the MRI probe. This increase normally causes a decrease of the solubility of the probes [74] and the shortening of the T_2 because of the reduced mobility of the system due to the increase of the molecular size. Thus, an overall attenuation of the MRI signal is observed.[75] In order to overcome these issues Kikuchi and co-workers have designed and synthesised a novel ^{19}F MRI probe in which a nanoemulsion of perfluoro-[15]crown-5 ether (PFCE) core was covered by a silica shell, obtaining a fluorine accumulated silica nanoparticle for MRI contrast enhancement (FLAME).[76] A PEGylated derivative, FLAME-PEG was also synthesised and its accumulation *in vivo* in mice bearing a tumour was demonstrated. As shown in Figure 13 strong ^{19}F MRI signals at the tumour site indicating a passive transport promoted by EPR were observed. In particular FLAME-PEG accumulated in liver and in the tumour. Interestingly, the non-PEGylated derivative FLAME-COOH accumulated only in the liver suggesting that it was immediately trapped by reticuloendothelial system (RES).

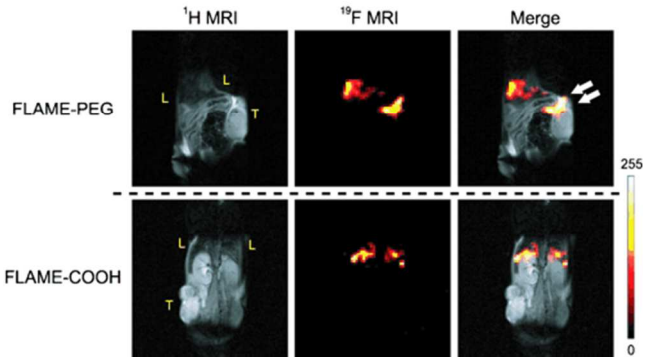

Figure 13 *In vivo* accumulation of FLAME-PEG and FLAME-COOH in tumour bearing mouse. The position of the liver and the tumour are indicated as L and T, respectively. Adapted with permission from Angew. Chem. Int. Ed., 2014, 53, 1008-1011. Copyright 2014 Wiley-VCH.

Optical Imaging (OI)

With respect to MRI, optical imaging (OI) is a complementary technique in which specific probes are excited by a radiation, usually in the visible or NIR regions, and emit light at a lower energy than the incident. OI is an emerging technology[77-79] which has great importance in early diagnosis, and, consequently, in the treatment of specific diseases.

One of the advantages concerns the fact that it does not use neither ionizing radiation nor radioactive materials, reducing patient radiation exposure and allows for repeated studies over time. Moreover, luminescence measurements are very sensitive (down to single molecule detection), versatile and easy to use, offering submicron spatial resolution and sub-millisecond temporal resolution.[80] This enables low detection limits and could permit the tracking of biological events to reveal the origin and growth of different pathologies. Optical imaging is a versatile and easy-to-use technique, due to relatively cheap instrumentation and availability of a variety of contrast agents for molecular targeting. It has been mostly used for cellular and intracellular imaging. However, with respect to *in vivo* imaging, this technique usually suffers from the attenuation of photon propagation in living tissue and poor signal to noise ratio due to tissue autofluorescence (normally, the resolution for OI is limited to 1-2 mm). For most clinical applications the use of NIR radiation (650-950 nm) would be desirable since it allows deeper penetration and a minimisation of the background effect due to blood and tissue absorption.[81]

Silica nanoparticles and in particular luminescent silica nanoparticles are ideal for the application in OI due to their chemical inertness, biocompatibility, transparency in the UV-Vis and NIR regions of the electromagnetic spectrum, high water dispersibility, and cellular membrane-penetrating capacity (endocytosis).[15-17, 82-86] Moreover, their surface can be easily modified by various functional groups such as aptamers, antibodies, peptides, folate and polymers for addressing the NPs towards specific tissues or cells.[87-92]

The common strategy for the fabrication of luminescent silica nanoparticles is immobilization or encapsulation of inorganic fluorophores (such as semiconductor quantum dots) or small organic dyes (such as rhodamine or fluorescein) into silica nanoparticles.[90] In this way luminescent silica nanoparticles that show a better photostability are obtained as the fluorophores are protected by the silica shell. This also limits the effect of the outside environment (such as oxygen, solvents and soluble species in buffer solutions) on the fluorescent dye contained in the nanoparticles.

The use of SiNPs for OI *in vitro* or *in vivo* depends on the class of fluorophores used to dope or functionalise the silica matrix.

Wang and co-workers reported several dye-doped silica nanoparticles used for fluorescence imaging at the cell and small animal levels.[93-99] Dye-doped SiNPs were covalently conjugated with different antibodies or ligands and then used to recognize selectively and efficiently antigens or receptors in several cell lines, such as SmIgG^{+}B lymphocyte for the immunodiagnosis of systemic erythema lupus,[94] HepG liver cancer cells,[93] and MCF-7 breast cancer cells.[98] In particular, the authors were able to identify liver cancer cells in a mixed cell system using galactose-conjugated fluorescent nanoparticles (GCFNPs) obtained by RuBpy-doped amino-modified fluorescent silica nanoparticles with lactobionic acid (LA)-conjugate through EDAC (-ethyl-3-(3-di methylaminopropyl)-carbodiimide hydrochloride) linkage.[96] The identification of liver cancer cells by GCFNPs was shown by confocal laser scanning microscopy imaging (CLSM) (Figures 14A and B). A bright red ring appeared only around the liver cancer cells, while the MCF-7-GFP control cells displayed green fluorescence (Figures 14C and D) because the specific asialoglycoprotein receptor did not exist on the breast cancer cell membrane surface. The control experiment with bare fluorescent nanoparticles (no galactose attached) did not show a detectable signal on the two cells. (Figure 14D).

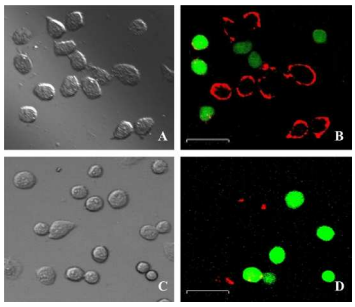

Figure 14 Recognition of liver cancer cells from mixed heterogeneous cells with GCFNPs by laser confocal microscope. (A and B) represented bright-field and fluorescent-field images of cells incubated with GCFNPs. (C and D) represented bright-field and fluorescent-field images of cells incubated with bare fluorescent nanoparticles. Scale bar, 50μm. Reproduced with permission from Talanta, 2007, 71, 833–840. Copyright 2007 Elsevier.

The RuBpy-doped SiNPs were also used on mixed cell system to prove the selective detection of colon cancer cells using silica nanoparticles conjugate with anti-human epithelial cell adhesion molecule (EpCAM) antibody. The fluorescence microscopy imaging demonstrated that the three kinds of Colo205 target colon cancer cells were distinguished from SW480 (EpCAM-deficient colon cells) and NCM460 (normal human colon cells). The membrane and nuclear staining showed the distribution and abundance of EpCAM in cells' membrane.[100]

Prasad and co-workers prepared a system based on small (20 nm) organically modified silica (ORMOSIL) nanoparticles to detect pancreatic cancer cells (Mia-PaCa cells). Rhodamine-B was incorporated in the particles that were conjugated with different

target molecules such transferrin or monoclonal antibodies (anti-claudin 4 and anti-mesothelin). The surface was functionalised with different active species (amines, carboxylate, etc.) and cellular uptake studies were carried out in pancreatic cancer *versus* normal (COS-1, fibroblast-like cells derived from kidneys of African green monkey) cells, using confocal laser scanning microscopy. Since neither the transferrin-receptor nor claudin 4 receptors are known to be overexpressed in COS-1, no uptake of the bioconjugated nanoparticles was observed in COS-1 cells, while a significantly higher uptake was observed in Mia-PaCa cells.[101]

In another study, Yang and co-workers[102] reported on SiNPs doped with fluorescein isothiocyanate (FITC) and PEG-conjugated to folate to obtain a folate receptor-targeted fluorescent nanoprobe (NPs(FITC)-PEG-Folate). The quantitative analysis of cellular internalization *in vitro* into different cancer cells showed that the delivery efficiency of KB cells (human oral carcinoma, folate receptor-positive cells) was more than six-fold higher than that of A549 cells (human lung carcinoma, folate receptor-negative cells).

Zhang, Liu and co-workers synthesized a bifunctional nanocomposite system consisting of Rubpy dye-doped silica nanoparticles ($DySiO_2$) and citrate-stabilized AuNPs ($DySiO_2$–(Au)*n*). After using an aptamer as thiolate dDNA conjugates, covalently bound to the surface of the nanoparticles *via* the self-assembled Au-S bond, they obtained aptamer modified nanoparticles that showed a good ability to recognise MCF-7 cancer cells.[103]

Dye-doped SiNPs could also be used for in situ sensing of intracellular physiological parameters change such as pH[104-106] or metal ions concentration.[107-110] In particular, a ratiometric pH nanosensor based on two-fluorophore-doped SiNPs containing a pH-sensitive indicator (fluorescein isothiocyanate, FITC) and a reference dye (RuBpy) for non-invasive monitoring of intracellular pH changes (Figure 15) was prepared. The pH nanosensor with an average diameter of 42 nm could be easily taken up by cells and showed excellent pH sensitivity, reversibility, and a dynamic range of pH 4-7 for biological studies. This pH nanosensor was used for monitoring pH changes in living cells by drug stimulation. Lysosomal pH changes in murine macrophages stimulated by chloroquine and the intracellular acidification in apoptotic cancer cells were monitored in real time. Furthermore, the relationship of intracellular acidification and apoptosis in HeLa cells induced by vincristine sulfate was studied which revealed that apoptosis was preceded by intracellular acidification.[97, 111]

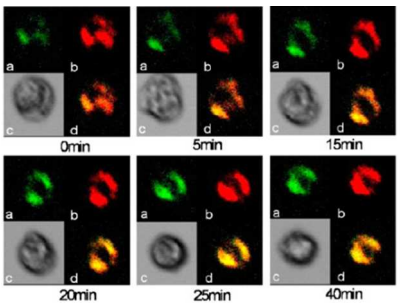

Figure 15 Change in lysosomal pH, as monitored by two-fluorophores doped SiNPs, in murine macrophages after treatment with chloroquine. Adapted with permission from Anal. Bioanal. Chem., 2007, 388, 645–654. Copyright 2007 Springer.

Zhang, Wei and co-workers[112] described luminescent silica nanoparticles obtained by the encapsulation of an aggregation-induced emission dye (derivatized from 9,10-distyrylanthracene with analkoxyl endgroup, named An18) *via* a modified Stöber method. In this method, octadecyltrimethoxysilane (C18-Si) and An18 were first self-assembled obtaining the core of the silica nanoparticles. Then another silicate precursor, tetraethoxysilane, was further coated on the luminescent core, obtaining the luminescent silica nanoparticles. The biocompatibility and cellular uptake behaviour of the An18-SiO_2 NPs were investigated to evaluate their potential for biomedical applications and the results demonstrated that the An18-SiO_2 NPs have a uniform spherical morphology (with diameter of 70–80 nm), high water dispersibility and excellent biocompatibility. The confocal laser scanning microscopy images of A549 cells incubated with 10 mg mL^{-1} of the An18-SiO_2 NPs for 3h are shown in Figure 16. The image obtained in phase-contrast mode (Figure 16A) indicated that cells still kept their normal morphology confirming the good biocompatibility of the An18-SiO_2 NPs. When cells were excited with a 488 nm laser, the cellular uptake of An18-SiO_2 NPs could be clearly distinguished due to the successful staining by the An18-SiO_2 NPs. Furthermore, many dark areas, which were surrounded by the An18-SiO_2 NPs areas, could also be found in the CLSM images, which are likely to be the locations of the nuclei of the cells (Figure 16 B,C).

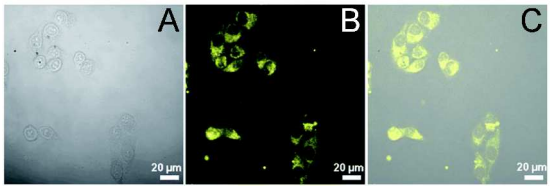

Figure 16. Confocal imaging of A549 cells. Cells were incubated with 10 mg mL^{-1} of An18-SiO_2 NPs for 3h. The laser excitation wavelength was 488 nm. Images were obtained in phase-contrast mode (A), in fluorescence mode (B) and in a merge mode (C). Adapted with permission from RSC Adv., 2014, 4, 10060–10066. Copyright 2014 RSC.

Prodi and co-workers designed and tested metastasis-targeted nanoparticles based on silica-condensed, alkoxysilane-derivatized fluorescent dyes, rhodamine (Rhod) and/or cyanine 5 (Cy5) within a micelle of the tri-block copolymer Pluronic®F127 (PF-127). A poly(ethylene glycol) shell embedding a dye-doped silica core was obtained (called single- and dual-SiNPs when one or two fluorescent dyes are present).[113] The poly(ethylene glycol) tails on the external face of the nanoparticles were functionalized with metastasis-specific peptides (H_2N-CGIYRLRS-COOH and H_2N-CGVYSLRS-CCOH) and the binding properties of the metastasis-targeted, dual-colour SiNPs on human samples of metastatic liver tissue have been investigated *ex vivo*. The 10-μm sections of OCT-frozen (optical cutting compound) human tissues were incubated with untargeted (control) and peptide-targeted (Rhod+Cy5)-SiNPs. The localization of specific fluorescent signals was evaluated *ex vivo* using confocal laser microscopy. Both CGIYRLRS- and CGVYSLRS-(Rhod+Cy5)-SiNPs showed binding selectivity for hepatic metastasis compared to normal liver and colon or primary colorectal cancer cells (CRC).[113]

Tan and co-workers have prepared a series of fluorescence resonance energy transfer (FRET) NPs functionalized with aptamers for the recognition of different cancer cells lines.[114] In comparison with single fluorophore-based systems, FRET has a relatively larger gap between the excitation and emission, and thus the crosstalk between the excitation light and the resulting fluorescence signals could be significantly reduced. In particular, silica nanoparticles were doped with three different dyes (a fluorescein and two rhodamines) to obtain single, dual and triple-dye containing NPs with different doping ratios that consequently showed different emission fluorescence under the same excitation wavelength (λ_{exc} = 488 nm). The NPs were targeted with various aptamers: sgc8 for CEM cells (human acute lymphoblastic leukemia cells, TDO5 for Ramon cells (human Burkitt's lymphoma cells) and T1 for Toledo cells (human diffuse large cell lymphoma). In Figure 17 it is well shown that each NP-aptamer conjugate could specifically bind to its corresponding target cell (NP(FAM)-T1 with Toledo (Figure 17A), NP(FAM-R6G)-sgc8 with CEM (Figure 17B), and NP(FAM-R6G-ROX)-TDO5 with Ramos (Figure 17C).

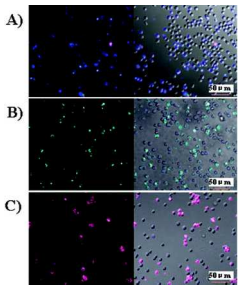

Figure 17 Confocal microscopy images showing a mixture of three cells (Toledo, CEM, and Ramos) incubated with one type of NP-aptamer conjugate: (A) NP(FAM)-T1, specific for Toledo; (B) NP(FAM-R6G)-sgc8, specific for CEM; and (C) NP(FAM-R6GROX)-TDO5, specific for Ramos cells. Reproduced with permission from Anal. Chem. 2009, 81, 7009–7014. Copyright 2009 American Chemical Society.

To overcome the drawback due the low penetration in the tissues, different types of NIR-SiNPs have been developed for *in vivo* optical imaging.

Wang and co-workers reported *in vivo* study of a NIR fluorescence probe encapsulating methylene blue (MB) alone in the phosphonate-terminated silica matrix (MB-doped SiNPs). The probe was injected in mice and emitted strong NIR fluorescence after administration (Figure 18A). The NPs subsequently accumulated in the RES such as liver and spleen (Figure 18B).[115] These NPs were also used for therapeutic purposes (see Therapy and Imaging section).

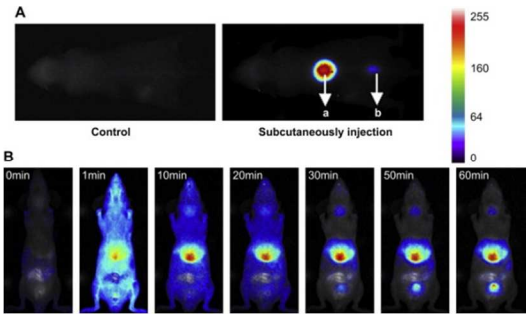

Figure 18 In vivo NIR imaging of mice with the (A) subcutaneous and (B) intravenous injection of MB-doped phosphonate-terminated SiNPs. Reproduced with permission from Biomaterials, 2009, 30, 5601–5609. Copyright 2009 Elsevier.

The same authors also reported Stokes shifting NIR fluorescent silica nanoparticles (LSS-NFSiNPs) based on FRET. The probe was prepared *via* contemporaneous doping of two highly water-soluble dyes, tris(2,2-bipyridyl)-dichlororuthenium(II) hexahydrate (RuBpy) and methylene blu (MB) in the silica nanoparticles (Figure 19A). The LSS-NFSiNPs showed strong fluorescence and large Stokes shift (>200 nm). Following the immediate intravenous injection of LSS-NFSiNPs, clear and bright fluorescence emitted from LSS-NFSiNPs could be easily visualized in the whole animal as shown in Figure 19B.[116]

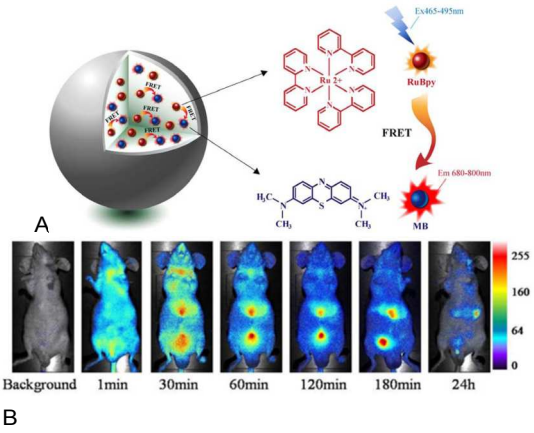

Figure 19 A) Schematic illustration of the LSS-NFSiNPs based on the principle of FRET from RuBpy to MB and the chemical structures of RuBpy and MB. B) Real-time *in vivo* abdomen FRET imaging of nude mice intravenously injected with the LSS-NFSiNPs. Adapted with permission from Anal. Chem. 2012, 84, 9056−9064. Copyright 2012, ACS.

An interesting example of multifluorophoric silica nanoparticles that showed unprecedented efficiencies in the energy-transfer processes was reported by Prodi and co-workers.[117] The same group has also proposed NIR emitting nanoparticles doped with a Cyanine 7 heptamethine dye, in the presence or not of a trialkoxylisane derivative of rhodamine B that showed a remarkable molar absorption coefficient (up to $3 \cdot 10^6$ M^{-1} cm^{-1}) in the 750–850 nm excitation window and a fluorescence quantum yield comparable to that of QDs.[118] Two or more different luminophores could be inserted in the same nanoparticle core with a one-pot reaction leading to systems allowing a 300 nm separation among the

excitation and the emission wavelengths. This strategy offered the possibility to use the same SiNPs on the same animal for both *in vivo* imaging and *ex vivo* microscopy. *In vivo* images revealed, just after the tail vein injection an increase of the signal well above the background emission measured in the pre-injection images using three kinds of NPs (N_C, N_{C+R}, N_R). The signal remained higher than the background three hours after injection and the biodistribution was well detectable (Figure 20).

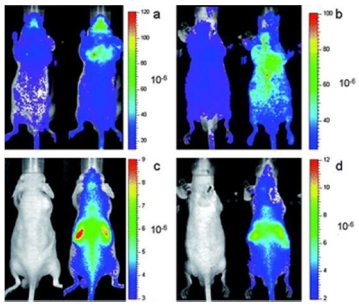

Figure 20 Average efficiency pre- and post-injection of NPs: N_R imaged with DsRed/DsRed filters (a), N_{C+R} imaged with DsRed/DsRed filters (b), N_C imaged with ICG/ICG filters (c), and N_{C+R} imaged with ICG/ICG filters (d). Reproduced with permission from Nanoscale, 2012, 4, 824–830. Copyright 2012 Royal Society Chemistry.

The same authors designed and synthesized two families of NIR-emitting Cy7-doped Pluronic-based core-shell silica-PEG SiNPs. The cyanine 7 (Cy7) dye was functionalised with a trialkoxysilane group for covalent linking to the silica matrix and high absorption coefficient with relatively high fluorescent quantum yields in the 800-900 nm range. These nanoparticles worked as efficient probes for *in vivo* mapping of regional lymph nodes in mice.[119]

Recently, in order to improve the depth penetration in OI, the two-photon fluorescence microscopy, a technique which provides three-dimensional (3D) cellular level resolution has been proposed. Belfield and co-workers, for example, synthesized PEGylated SiNPs containing a two-photon adsorbing and aggregation-enhanced NIR emitting pyran derivative (2-(2,6-bis((E)-2-(7-(diphenylamino)-9,9-diethyl-9Hfluoren-2-yl)vinyl)-4H-pyran-4-ylidene)malononitrile (DFP) encapsulated in silica nanoparticles whose surface was functionalized with folic acid. The targeting ability of these SiNPs was demonstrated by intravenous injection into mice to detect HeLa tumour (Figure 21). Indeed the nanoparticles not only targeted the tumour but also penetrated deeply into the cancer parenchyma as demonstrated by *ex-vivo* cellular two photon fluorescence microscopy.[120]

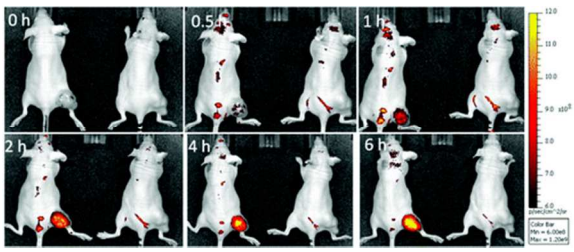

Figure 21 Representative whole-body *in vivo* fluorescence images of mice bearing HeLa tumours. The mice were intravenously administered with DFP-containing folate SiNP conjugate (left) or DFP-containing SiNP without folic acid derivatization (right) at 3 nmol/g body weight, and the fluorescence signal was monitored at different time points post-probe administration. Reproduced with permission from Bioconjugate Chem. 2011, 22, 1438–1450. Copyright 2011 American Chemical Society.

All examples reported above in this section and the majority of those reported in the literature concern solid silica nanoparticles (SiNPs), however mesoporous silica nanoparticles (MSNs) have also been employed for the development of OI agents.[121-126] In particular, Achilefu, Sokolov and co-workers[124] reported ultrabright fluorescent meso(nano)porous silica nanoparticles of 28 nm in diameter incorporating polymethine cyanine NIR fluorescent dye LS277. When excited in NIR spectral region (>700 nm), these particles were up to 4x brighter than QD800 commercial quantum dots emitting at 800 nm, easily internalized by 4T1luc breast tumour cells, and remained bright for more than 9 weeks whereas the dye was completely bleached by that time.

Positron Emission Tomography (PET)

Positron Emission Tomography (PET) is based on the preparation of specific molecular imaging probes labelled with positron-emitting radioisotopes.[127] Recently the strategy of functionalise silica NPs with radioisotopes have been developed.[128] *In vivo*, PET allows bioimaging and possesses the advantages of unlimited depth penetration. It allows biodistribution studies of the radiolabelled NPs via detection and quantification of picomolar amounts of radiotracers.[129-131] Moreover, PET is a highly sensitive clinical imaging modality for tumour early-diagnosis. PET has a broad range of probes. The physical half-life ($T_{1/2}$) of the radionuclide which is introduced into silica nanoparticles for PET imaging plays a crucial role for measurements in the desired time frame. Table 1 gives an overview of radiolabeled silica nanoparticles used in PET imaging described in this review.[132-136]

Table 1 Overview of functionalised silica NPs for PET imaging

Radio isotope	$T_{1/2}$	NPs	Diameter (nm)	Ref.
^{18}F	109.8 min	^{18}F-DBCOT-PEG-MSNs	100-150	132
^{64}Cu	12.6 h	^{64}Cu-NOTA-mSiO_2-PEG-TRC105; DyeZW800-MSN-Gd-^{64}Cu	168±8.2; 76.8±8.3	133 136
^{89}Zr	78 h	^{89}Zr-DFO-MSNs	180	134
^{124}I	4.18 days	^{124}I-ORMOSIL-dye	20-25	135

For measurement within a short time frame after intravenous administration, short-lived radionuclides have been applied. Due to its ideal imaging characteristics (positron energy $E_{\beta+}$,

max = 635 keV) and good availability, ^{18}F ($T_{1/2}$ = 109.8 min) has been used as a suitable PET nuclide *in vivo*.[130, 137-139]

Kim *et al.*[132] described an efficient ^{18}F-labelled silica nanoparticle for PET imaging based on the strain-promoted alkyne azide cycloaddition (SPAAC) conjugation of aza-dibenzocyclooctyne (DBCO) *in vivo* using ^{18}F fluoropentaethylene glycolic azide. The authors firstly synthesized DBCO-based PEGylated MSNs (DBCO-PEG-MSNs) with size of 100-150 nm. The DBCO group as an azide acceptor was introduced into a long chain PEG-amine moiety. To investigate the SPAAC reaction rate and the feasibility of the copper-free click reaction *in vivo*, DBCO-PEG-MSNs was reacted with ^{18}F fluoropentaethylene glycolic azide under physiological conditions (in PBS, 36.5°C, pH 7.4), affording ^{18}F-labeled azadibenzocyclooctatriazolic PEG-MSNs (^{18}F-DBCOT-PEG-MSNs) in almost quantative radiochemical yield. The modified nanoparticles were injected intravenously into mice bearing a subcutaneous U87MG (a human glioblastoma) tumour and after 24h the radiotracer was injected and PET images were acquired (Figure 22B). Another group of mice were not injected with the DBCO-PEG-MSNs but only with the radiotracer (Figure 22C). Comparison between the two groups after 2h showed similar uptake in all the tissues except in the tumour whereas the pre-targeted mice showed significantly higher tumour uptake than the non-pre-targeted mice by forming ^{18}F-DBCOT-PEG-MSNs within 2h after injection, by SPAAC conjugation reaction *in vivo*. Furthermore, increasing the amount injected of modified nanoparticles for pre-targeting, the radiotracer exhibited a higher tumour uptake, improving the tumour to blood ratios.

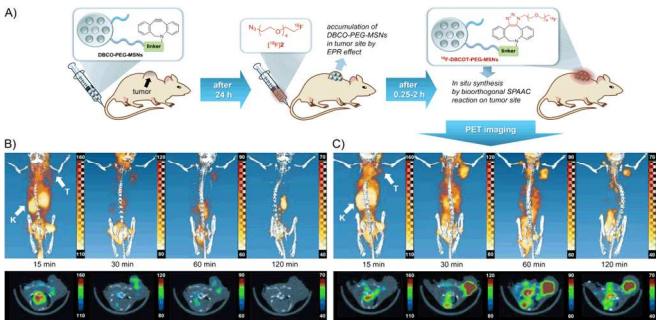

Figure 22 A) Pre-targeting procedure for *in vivo* synthesis of ^{18}F-labeled azadibenzocyclooctatriazolic PEG-MSNs (^{18}F-DBCOT-PEG-MSNs). B)C) 3D PET images (upper) and transversal section (lower) of ^{18}F-labeled azide in a U87MG tumour-bearing mouse given only the radiotracer alone (non-pre-targeted B) or a mouse given the DBCO-PEG-MSNs 24h earlier (pre-targeted C), T=tumour, K=kidney. Reproduced with permission from Angew. Chem. Int. Ed., 2013, 52, 10549 – 10552. Copyright 2013 Wiley-VCH.

The half-life of ^{18}F is only 109.8 minutes, which puts a limit to the maximum observation time for single administration. A relevant improvement would, therefore, be the development of MSNs-based carriers for the application of PET with longer half-lives $T_{1/2}$. Among metals, few radiometals have been used for labelling silica NPs, including ^{64}Cu ($T_{1/2}$ = 12.6 h, $E_{\beta+}$, max = 655 keV) and ^{89}Zr ($T_{1/2}$ = 78 h, $E_{\beta+}$, max = 909 keV). Labelling NPs with a radiometal requires a chelator which forms stable complexes with the radiometal. The most widely used chelators are the macrocyclic ligands 1,4,7,10-tetraazacyclododecane-1,4,7,10-tetaacetic acid (DOTA) and 1,4,7-triazacyclononane-1,4,7-triacetic acid (NOTA).

Cai *et al.*[133] described the development of functionalized MSNs ^{64}Cu-NOTA-mSiO_2-PEG-TRC105 for actively targeted PET imaging and drug delivery in 4T1 murine breast tumour-bearing mice. TRC105 is a human chimeric monoclonal antibody which binds to endoglin.[140] Targeted ^{64}Cu-NOTA-mSiO_2-PEG-TRC105 and non-targeted ^{64}Cu-NOTA-mSiO_2-PEG were injected intravenously into two groups of 4T1 murine breast tumour-bearing mice. *In vivo* PET imaging and biodistribution studies showed that MSNs concentrated mainly in the tumour site (yellow arrowhead in Figure 23). A certain uptake was also observed in liver, intestine, kidneys, and spleen. Targeted ^{64}Cu-NOTA-mSiO_2-PEG-TRC105 accumulated in the 4T1 tumour-bearing mice 2-fold more than the non-targeted ^{64}Cu-NOTA-mSiO_2-PEG (Figure 23a and 23b, respectively) *via* both the EPR effect and TRC105-mediated binding to tumour vasculature endoglin indicating that TRC105 conjugation was the controlling factor for enhanced tumour uptake of ^{64}Cu-NOTA-mSiO_2-PEG-TRC105.

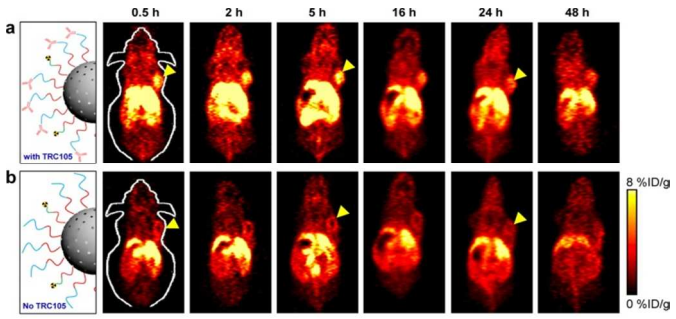

Figure 23 PET images of tumour-bearing mice after injection of a) targeted ^{64}Cu-NOTA-mSiO_2-PEG-TRC105 or b) non-targeted ^{64}Cu-NOTA-mSiO_2-PEG. Adapted with permission from ACS Nano, 2013, 7, 9027 – 9039. Copyright 2013 ACS.

An example of radiolabeled NPs containing ^{89}Zr was reported by Reske, Linden *et al.*[134] who described radiolabeled NPs ^{89}Zr-DFO-MSNs (DFO = desferrioxamine) dispersed in biological media. Radiolabeled NPs ^{89}Zr-DFO-MSNs or radiolabeled $^{89}Zr^{4+}$ as a salt solution, were injected into the tail vein of two groups of nude mice model carrying a prostate cancer tumour (LNCaP C4-2). After 1h, the authors performed biodistribution studies. The nanoparticles gave a strong PET signal *in vivo* (Figure 24A). While the ^{89}Zr-DFO-MSNs accumulated mainly in the liver, spleen and lung, $^{89}Zr^{4+}$ administered in free form was present largely in the blood and distributed homogeneously over all the organs (Figure 24B). However, no accumulation of ^{89}Zr-DFO-MSNs was observed in the tumour, due to a lack of optimization of the nanoparticles for maximum tumour uptake.

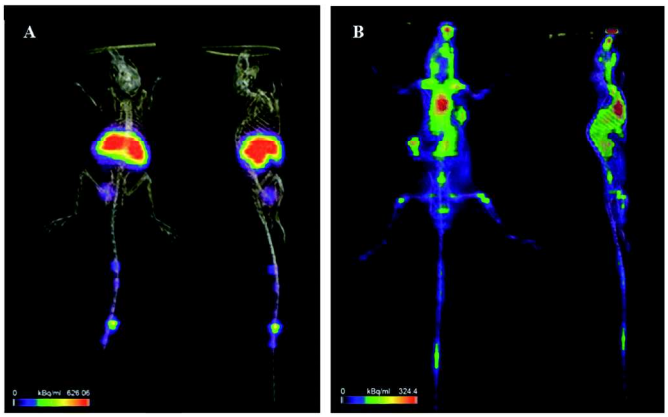

Figure 24 PET image of mice taken 1 h after injection of A) ^{89}Zr-DFO-MSNs, B) $^{89}ZrCl_4$ solution. Reproduced with permission from Nanoscale, 2014, 6, 4928–4935. Copyright 2014 RSC.

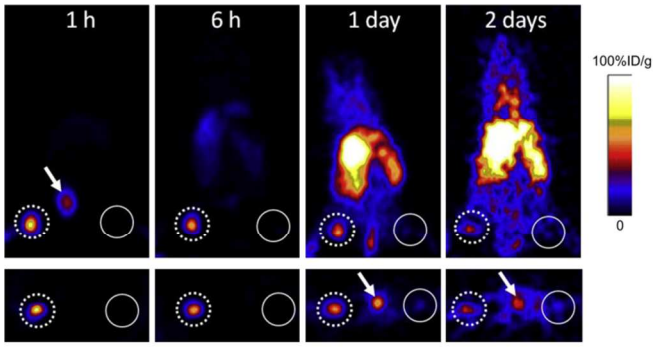

Figure 25 PET imaging of T-SLNs (square dot) and N-SLNs (solid line) after injection of particles, in a 4T1 tumour metastatic model. Arrow denotes bladder. Top: cross section; bottom: transverse section. Adapted with permission from Biomaterials, 2012, 33, 4370–4378. Copyright 2012 Elsevier Ltd.

PET has also been combined with others bioimaging techniques.[135, 136] Prasad *et al.*[135] reported the synthesis of ORMOSIL nanoparticles conjugated with near-infrared (NIR) fluorophores and radiolabeled with ^{124}I for optical and PET imaging *in vivo*. Biodistribution studies based on the acquisition of fluorescence emission of the conjugated fluorophore and the gamma emission of the conjugated ^{124}I of the ORMOSIL nanoparticles injected in non tumoured mice suggested an accumulation of the nanoparticles in spleen, liver and lungs. In these studies, the half-life of the ^{124}I (4.18 days) was sufficient to perform decay-corrected gamma counting until 2 weeks post injection. However the ^{124}I, which was tagged on the surface of the nanoparticles *via* an amide bond, could be easily hydrolysed by enzymes in the liver.[141]

Chen *et al.*[136] designed a mesoporous silica triple-modal imaging nanoprobe (DyeZW800-MSN-Gd-^{64}Cu) for *in vivo* long-term PET imaging of tumour draining sentinel lymph node (T-SLNs). The authors integrated into MSNs by different conjugation strategies three imaging tags including near-infrared (NIR) dye ZW800, T_1 contrast agent Gd^{3+} and positron emitting radionuclide ^{64}Cu. The radiolabeled MSNs were obtained by chelation of the radionuclide with the functional groups DOTA-NHS on the surface and in the mesoporous channels. ^{64}Cu labeled-MSN-probes were injected in rat. It was observed by PET imaging that the radioactivity accumulation in tumour metastatic SLNs (T-SLNs) was much higher than in normal contra-lateral SLNs (N-SLNs) were almost no signal was observed (Figure 25). The modified MSN-probe possessed the ability to track T-SLNs changes induced by tumour cell migration, confirming the feasibility of these MSN-probes as contrast agents to map SLNs and identify tumour metastasis.

X-Ray Computed Tomography (CT)

X-ray imaging has been used in clinical practice for more than half a century and nowadays computed tomography (CT) is one of the most commonly used diagnostic tool. Images in CT are obtained when tissues absorb X-rays differentially as they pass through the body. During the data acquisition, the X-ray tube rotates around the body, and then data are processed by dedicated computer hardware which gives high-resolution 3D structure details of tissues. The CT images show the absorption of X-ray beams which is related to the density of the different tissues.[142] In CT, tissue density that corresponds to different shades of grey is expressed in Hounsfield Units (HU). Hard tissues like bones, soft tissues, and air cavities are clearly visible and recognizable. However, different soft-tissue classes, such as tumours, cannot be well distinguished. This limits diagnostic sensitivity when investigating pathologies such as cancer. Thus, it becomes necessary to administer contrast media to delineate soft-tissue organs.

Nowadays, hydrophilic iodinated molecules are clinically used as radiographic contrast agents.[143] Although iodinated agents are generally safe,[144] a severe adverse reaction sometimes occurs caused by their high osmolality and viscosity.[145] Moreover, the quick renal clearance of iodinated agents would lead to a very short imaging duration, which may result in the difficulty in the target-specific imaging. Therefore, a distinguishable CT contrast image can only be obtained under a large dosage of iodinated compounds, which may cause potential serious renal toxicity.[146]

Nanoparticles that have prolonged circulation times and therefore remain in the bloodstream,[147, 148] could be used as contrast agents in CT imaging. Moreover, the attenuation of the X-rays energy caused by CT contrast agents depends on the interaction between the X-rays and the inner shell electrons of the contrast agents. Thus, an atom with a high atomic number has a high attenuation coefficient.

In the last decade, research activity has been devoted to the development of nanoparticles as CT contrast agents.[149-152] These nanoparticles can be applied to produce long-lived CT contrast in the blood vessels and to perform targeted imaging.

Nowadays, incorporation of iodinated organic compounds into a nanoparticle has been successfully applied *in vivo*.[153, 154] The design principle for many of these nanomaterials has been to enhance localized iodine concentrations, resulting in higher local contrast compared to conventional water-soluble compounds. Despite prolonged *in vivo* circulation time compared to iodinated molecules, iodine-conjugated nanoparticles are still limited by iodine loading through surface covalent conjugation. Due to these drawbacks of iodinated compounds, nanoparticles with high atomic number (high-Z) metal elements as potential CT contrast agents have recently been used.[150-152]

In the last decade, there has been substantial interest in gold nanoparticles (AuNPs) based contrast agents for *in vivo* CT imaging.[155-158] Gold (Z = 79) has a higher atomic number than iodine (Z = 53), and thus, a better contrast with a lower X-ray dose can be achieve.[159] Moreover, gold is chemically inert and it is considered to be non-toxic *in vivo*.[160, 161] Very recently, silica-modified gold nanorods[162, 163] and silica-modified gold nanoparticles[164] have been used as contrast agents for CT imaging. Cui *et al.*[162] reported a multifunctional nanoprobe of folic acid-conjugated silica-coated gold nanorods (GNR-SiO_2-FA) for radiation therapy (RT)-photothermal therapy (PTT), and *in vivo* CT imaging (see also section Imaging and Therapy). After intravenous injection in mice of the contrast media GNR-SiO_2-FA dispersed in PBS, the subcutaneous injection site displayed a strong CT signal and an increase of the HU values at the injection site was observed compared to the values of other tissue (such as bone or muscle) (Figure 26C and 26D), indicating that the synthesized GNR-SiO_2-FA is effective for *in vivo* CT imaging.

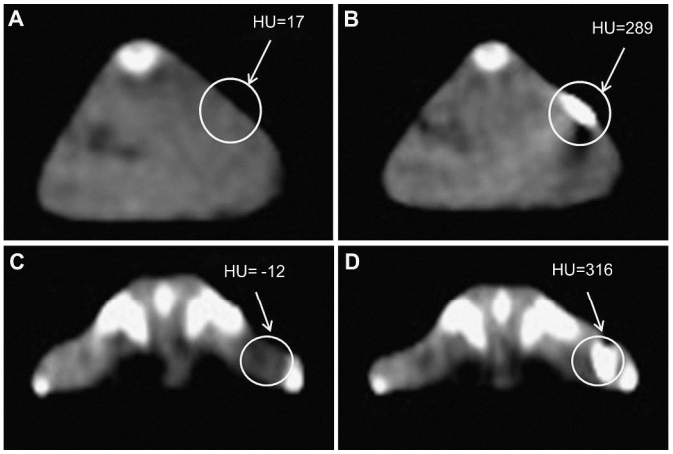

Figure 26 In vivo CT images of mice before injection (A, C) and after injection with GNR-SiO_2-FA suspended in PBS (B, D). A, B: transverse image of the back, C, D: transverse image of the buttock. Reproduced with permission from Biomaterials, 2011, 32, 9796–9809. Copyright 2011 Elsevier Ltd.

Moreover, the authors injected GNR-SiO_2-FA nanoprobe in mice bearing gastric cancer MGC803 cells. Compared to healthy tissue, the GNR-SiO_2-FA nanoparticles gradually accumulated at the tumour site demonstrating significant uptake and high targeting specificity of the CT media.

The same authors also reported silica-coated gold nanorods for dual imaging by CT and optical imaging.[163] Zhou, Ren *et al.* synthesized non-targeted mesoporous silica-coated gold nanorods loaded with an organic NIR dye indocyanine green (ICG-loaded Au@SiO_2). CT scanning showed that ICG-loaded Au@SiO_2 could provide significant contrast enhancement and the nanoparticles were still present in the gastric cancer tissue up to 12h post intratumoural injection.

Mulder *et al.* reported trimodal gold/silica nanoparticles coated by a lipid-based layer, conjugated with paramagnetic Gd−chelates and near-infrared (NIR) fluorescent dyes Cy5.5 for combined MRI, CT and optical imaging.[164] *In vivo* CT imaging of mice livers was performed at 24h intravenously post-injection of lipid-coated gold/silica nanoparticles at a dose of 0.15 nmol kg^{-1}. The electron-dense gold core enables its detection. CT side views of the whole mouse body prior to and post nanoparticles administration revealed a 50% X-ray attenuation enhanced intensity of mice livers (Figure 27).

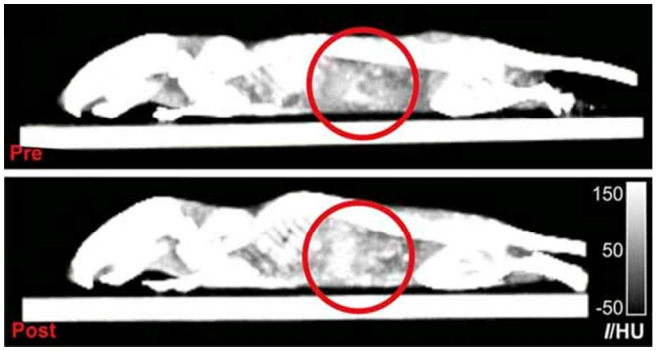

Figure 27 Side view 3D CT projections of mice abdomens prior (up) to and 24 h post injection (down) of the lipid-coated gold/silica nanoparticles. Red circles indicate regions with enhanced contrast. Adapted with permission from Contrast Media Mol. Imaging, 2010, 5, 231 – 236. Copyright 2010 Wiley-VCH.

High atomic number elements are potentially interesting candidates for the design of CT contrast agents and NPs based on Bi (Z = 83)[165] or Yb (Z = 70)[166, 167] have been reported as contrast agents for *in vivo* CT. Also, to increase biocompatibility of nude inorganic NPs and further functionalization of the NPs for multimodal applications, inorganic nanoparticles have been coated into silica shell.[168] Very recently silica-coated lanthanide nanoparticles as contrast agents for *in vivo* CT have been reported.[169-173]

Silica-coated $BaYbF_5$ nanoparticles passivated with PEG-silane ($BaYbF_5$@SiO_2@PEG) containing two contrast elements (Ba and Yb) were reported as the first example of binary contrast agents for CT by Lu *et al.* [169] *In vitro* studies showed low cytotoxicity of the nanoparticles. The authors showed an enhancement in X-ray attenuation of $BaYbF_5$@SiO_2@PEG compared to Iobitridol and $NaYbF_4$@PEG. *In vivo,* high resolution blood pool CT images were obtained after intravenous injection of $BaYbF_5$@SiO_2@PEG solution into a rabbit. At 10 min post-injection, various blood vessels were clearly visualized in CT images (Figure 28). The high colloidal stability arising from PEG coating enabled a long retention time

of the NPs in the vasculature and after 1h, the bright signal of these blood vessels remained.

Figure 28 High-resolution blood pool 3D CT images of a rabbit collected at 10 min after intravenous injection of $BaYbF_5$@SiO_2@PEG solution. Arrows indicate several great vessels: (1) auricular vein, (2) jugular vein, (3) carotid artery, (4) subclavian vein, (5) axillary vein, (6) aortic arch, (7) inferior vena cava, and (8) aorta. Reproduced with permission from Advanced Healthcare Materials, 2012, 4, 461 – 466. Copyright 2012 Wiley-VCH

Moreover, silica-coated lanthanide doped upconversion nanoparticles (UCNPs) were used for dual-modality imaging of upconversion luminescence (UCL) and CT.[170, 173] These upconversion nanoparticles showed much greater CT contrast effects than iodinated CT contrast agents.

Cui *et al.* [170] designed contrast agent based folic acid conjugated silica-modified LaF_3:Yb,Tm upconversion nanoparticles (UCNPs@SiO_2-FA) for simultaneously targeting dual-modality imaging of UCL and CT. 10 mg/mL of UCNPs@SiO_2-FA were intradermal injected into the right paw of a mouse and *in vivo* CT images were acquired (Figure 29). The subcutaneous injection site displayed an enhanced positive-contrast compared to that of other soft tissues, which was attributed to the strong X-ray attenuation induced by lanthanide elements. Meanwhile, the HU value of the injection site was higher than the values of other tissues (such as bone, muscle), indicating that the synthesized NPs were effective for CT imaging *in vivo*.

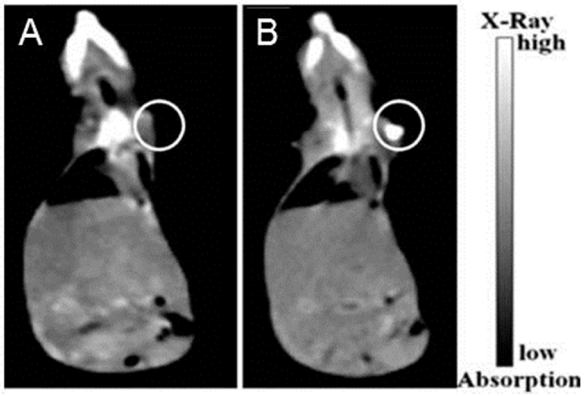

Figure 29 *In vivo* lymphatic node CT images of mice. Prior injection (A) and 1h post-injection (B) of UCNPs@SiO_2-FA (100 μL, 10 mg/mL) injected into the right paw of the mouse. Adapted with permission from J. Phys. Chem. B, 2012, 116, 14062 – 14070. Copyright 2012 ACS.

Yuan, Lu *et al.*[173] synthesized $NaYF_4$:18%Yb^{3+},2%Er^{3+} nanoparticles, encapsulated in a silica shell. Amino-2,4,6-triiodoisophthalic acid (AIPA), an organic iodine molecule, was then attached to their surface to improve CT contrast and finally NPs were linked to PEG to improve stability to obtain UCNPs@SiO_2-I/PEG. *In vitro* CT images demonstrated that the total contrast of UCNPs@SiO_2-I/PEG nanoprobes derived from both the presence of the iodine and the rare earth elements (Y, Yb, and Er). After intravenous injection of UCNPs@SiO_2-I/PEG nanoprobes aqueous solution into a rat, *in vivo* CT images showed prolonged circulation time of the nanoprobes and enhancement of liver contrast of the rat after 30 min.

Furthermore, silica-coated lanthanide nanoparticles were used as trimodal (CT/MRI/UCL) imaging probe. Feng, Li *et al.*[171] synthesized $NaLuF_4$:Yb^{3+},Tm^{3+}@SiO_2-DTPA-Gd nanoparticles (UCNP@SiO_2-GdDTPA) with $NaLuF_4$:Yb^{3+},Tm^{3+} as the core, SiO_2 as the shell layer, and the DTPA-Gd^{3+} complex as the surface ligand, for NIR-to-NIR UCL, MRI and CT trimodal imaging. The authors performed *in vivo* viscera CT imaging of the abdomen of a Kunming mouse with intravenous injection of 3 mg/day UCNP@SiO_2-GdDTPA every day for 1 week. The structures of the kidneys, liver, stomach and intestines could be distinguished clearly by serial coronal CT images. Thus, the nanoparticles could be potentially applied as a long-term CT imaging contrast agent *in vivo*.

Shi *et al.*[172] synthesized NaY/GdF_4: Yb, Er, Tm @SiO_2-Au@PEG_{5000} nanoparticles by coating lanthanide core nanoparticles with an amine-functionalized SiO_2 shell, then grafting the particles with PEG moieties and finally adding CT media gold nanoparticles. *In vivo* CT-images showed that after subcutaneous injection of the probes into the tumour, the HU value of the tumour site increased from 40.86 HU to 102.34 HU while the HU value of the soft tissue site remained almost unchanged (65.33 to 61.00). The authors indicated that these NPs might be a promising contrast agent for CT imaging.

Ultrasound Imaging (US)

Ultrasound imaging is a safe, fast and non-invasive medical imaging modality which has been widely used in clinical diagnosis.[174] Microbubbles generated by agitating saline solution have been used as a contrast agent for ultrasound since the 1970's. These microbubbles, which can transform into acoustic-sensitive gas bubbles during ultrasound scattering, have been extensively researched for ultrasound imaging.[175] Gas-filled microbubbles have been developed to enhance the ultrasound signal. Unfortunately, these microbubbles dissolve and collapse within seconds after injection into the bloodstream because of the effect of Laplace pressure, blood pressure, oxygen metabolism, and exposure to ultrasound energy.[176]

Since two decades, various strategies have been reported for targeted ultrasound imaging,[177, 178] and a new generation of contrast agents for ultrasound imaging consisting of gas-filled (air or perfluorocarbon (PFC)) microbubbles encapsulated by soft-shell particles made of surfactants,[179] lipids,[180, 181] or polymers[182, 183] has been reported. These organic microbubbles have been clinically used and are able to oscillate and vibrate

when insonified with ultrasound frequency within the diagnostic range. *In vivo,* differences in the indices of refraction between liquid media and gas cause the particles to appear brighter than the background and high resolution images can be obtained. Microbubbles have shown to enhance the contrast of ultrasound imaging, however, conventional ultrasound microbubble imaging agents which use soft shells have been shown to persist for only 15 min in tissues. Indeed, their large particles sizes (usually micrometer), broad size distribution and instability make it difficult to obtain tumour imaging or diagnosis of diseases at their early stages due to their inability to pass through endothelial barriers and accumulate at tumour sites.[176, 184] Moreover, all currently microbubbles lack the ability to be functionalized with tumour-targeting moieties.

Silica nanoparticles have been subject to recent studies as contrast enhancing agents for ultrasound imaging and have been successfully exploited as ultrasound contrast agents at conventional diagnostic frequencies.[185, 186] Their contrast agent enhancement potential is based on the inhomogeneity they introduce in the target tissue due to a generally higher mismatch with the physiological environment compare to soft shells particles.

Recently developed hollow silica nano-/micro-spheres or hollow mesoporous silica nanoparticles (HMSNs),[187, 188] showed excellent echogenic behaviours and greater advantages than traditional organic microbubbles due to their extremely high stability under the ultrasound exposure and adequate particle sizes. Mattrey, Kummel, Trogler *et al.*[188] synthesized hollow hard shell silica particles of 200 nm and 2 micron diameter filled with perfluorocarbon (PFC) gas. The particles behaved as an efficient contrast agent for colour Doppler ultrasound imaging in human breast tissue. The gas filled silica micro and nanoshells injected directly in tissue were shown to persist for several days and could be readily imaged in human breast tissues in 3D after injection.

Moreover, HMSNs have been recently preliminarily employed as the contrast agent for ultrasound imaging of small tumours. Wu *et al.*[189] developed gas filled hollow boron-dopped silica particles, which can be used for continuous ultrasound imaging. The particles were synthesized using a polystyrene template and subsequently calcinated to create hollow, rigid nanoporous microspheres which were filled with perfluoropentane vapour. *In vitro* and *in vivo* experiments demonstrated that the signal generated by these microshells remained detectable for several days. The authors also studied their persistence *in vivo* ultrasound imaging in tumour bearing mice. The silica particles (200 µg of 2 µm silica shells diluted into 3 ml of saline solition) were injected into mice with intraperitoneal IGROV-1 ovarian tumours and were tested for their ability to accumulate within the tumour and be imaged by contrast enhanced ultrasound (CEUS). The signal generated by the particles could be seen specifically in the tumour 1h after injection (Figure 30).

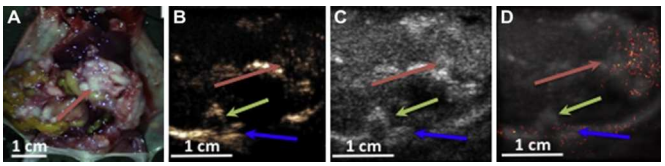

Figure 30 A) Photo of dissected mouse with an intraperitoneal IGROV-1 ovarian tumour. B, C and D) Images of the particles through a cross section of the tumour 1h after injection, (B: CPS imaging), (C: B-mode), (D: Overlay image using several frames from CPS imaging and B-mode). For all the images, the red arrow points to the tumour, the green arrow points to the spinal column and the blue arrow points to the bottom of the mouse. Reproduced with permission from Biomaterials, 2012, 33, 5124–5129. Copyright 2012 Elsevier Ltd.

Very recently, mesoporous silica nanoparticles functionalized with monoclonal antibody Herceptin have also been used as an effective breast-cancer targeting ultrasound contrast agent.[190]

Hollow mesoporous silica nanoparticles (HMSNs) have been used as-prepared (without filling the silica nanoparticles with gas) for ultrasound imaging. Functionalized PEGylated hollow silica microspheres (PEG-HSS),[191] and functionalized hollow silica microspheres ($HSMS\text{-}NH_2$)[192] showed excellent echogenic behaviours. Li, Yang *et al.* synthesized PEG-grafted hollow silica spheres (PEG-HSS) of 1250 nm in diameter prepared from coating a thin layer of amino functionalized silica on a monodisperse positive charged polystyrene template, removing the template in THF solution, and further coupling the HSS with methoxy polyethylene glycol propionic acid (mPEG-COOH).[191] The *in vitro* studies established that the as-prepared PEG-HSS demonstrated a very good ultrasound imaging effectiveness in both physiological saline solution and human blood, at the optimized conditions of 6.0 MHz for the acoustic frequency, 0.060-0.1 for the mechanical index and 0.60-0.80 $mg.mL^{-1}$ for particle concentrations. The authors could also obtained clear *in vivo* 2D and CEUS mode images of a testicle of a male rat for 20 min after injection of as-prepared PEG-HSS (Figure 31), showing that the hollow silica NPs had great potential as a novel ultrasound contrast agent.

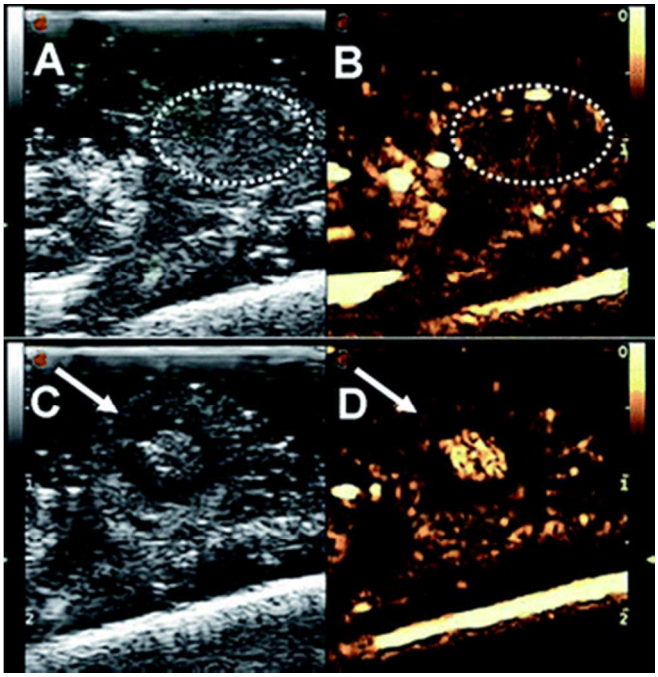

Figure 31 In vivo ultrasound images of male rat spermary in 2D (A,C) and CEUS mode (B,D) before (A,B) and after (C,D) intra-testicular injection of 500 μL of PEG–HSS (0.80 mg mL^{-1}) physiological saline suspension. The local testicular tissue is represented by a white circle and an arrow on the images. Reproduced with permission from J. Mater. Chem., 2011, 21, 6576–6583. Copyright 2014 RSC.

Ultrasound imaging has been used in combination with MRI.[193, 194] Chen, Li, Shi *et al*.[193] synthesized monodispersed manganese oxide-based integrated hollow mesoporous silica nanoparticles (MnO_x HMSNs) for *in vitro* and *in vivo* ultrasound tumour imaging. The HMSNs showed well-defined spherical morphology with large hollow interiors and great stability in saline solution after further PEGylation of the surface. *In vivo* studies were carried out employing New Zealand white rabbits bearing VX2 liver tumour as the disease model. Significant contrast enhancement at the tumour site could be found after puncture administration of HMSNs under the ultrasound guidance compared to the control rabbit under both harmonic and B-mode (Figure 32C and 32D, respectively). These *in vivo* results suggested that HMSNs could potentially function as ultrasonography contrast agent for real-time guidance to image the tumour tissue margins during surgical process.

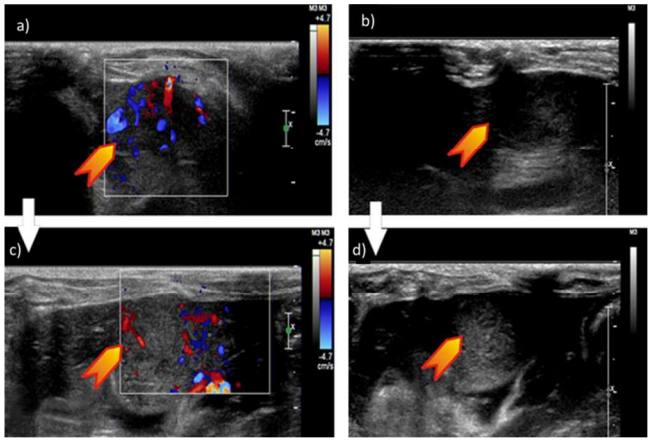

Figure 32 *In vivo* ultrasound images of liver tumour VX2 bearing rabbits, pre- (a, b) and post- (c, d) puncture injection of PEGylated MnO_x-HMSNs in harmonic-mode (left) and conventional B-mode (right). Adapted with permission from Biomaterials, 2012, 33, 7126–7137. Copyright 2012 Elsevier Ltd.

Multimodal Imaging

Silica nanoparticles are ideal platforms for the development of multimodal imaging probes, i.e probes that allow the use in the same system of two or more different techniques, MRI/OI, MRI/PET, OI/CT, CT/PET, just to cite the most common. Indeed, numerous examples of materials suitable for multimodal imaging have been developed and this topic have been reviewed in the past.[4, 84, 195-202] Some examples have already been cited in the previous sections[48, 52, 61, 64, 66, 70, 135, 136, 162-164, 170-173, 193, 194] and will be briefly described in the next section.[203-208] For this reason in this section, we will focus only on a selection of the most recent examples (years 2013-2014) reported in the literature regarding multimodal silica-based NPs.

In this context, multimodal imaging probes that combine MRI with OI are quite appealing. Indeed, although MRI is the most powerful tool for diagnosis nowadays and most hospitals are equipped for this analysis, however, as mentioned above, it lacks in sensitivity and contrast agents need to be used. On the other hand, OI offers the advantages of higher sensitivity and spatial resolution than MRI. The combination of the two techniques allows to overcome the specific limitations. An example of multimodal MRI/OI system have been described by Muller and co-workers.[209] Gd-DTPA was covalently grafted to the surface of the silica nanoparticles while tris-2,2`-bipyridyl ruthenium complex was entrapped inside. The NPs showed a strong fluorescent emission at 587 nm when excited at 455 nm and fluorescence was clearly observed up to a concentration of silicon 53.25 μM corresponding to a concentration of Gd^{3+} 7.75 μM. Nuclear Magnetic Relaxation Dispersion (NMRD) profile showed higher relaxivity values for the NPs compared to the Gd^{3+} complex alone and a hyperintense signal of T_1-weighted images at a concentration of Gd^{3+} 77.5 μM was observed.

Müller, Jing and collaborators have reported on silica nanoparticles incorporating Gd^{3+} and Tb^{3+} obtaining a material

that showed both visible photoluminescence and T_1 contrast enhancement.[210]

A similar system, consisting in mesoporous core-shell silica-based NPs (YGO-Bmnc) have been described.[211] They consist in a nanocore of $(Y,Gd)_2O_3:Eu^{3+}$ coated with mesoporous silica. In this system, Gd^{3+} is the MRI contrast agent, Eu^{3+} is the light emitting ion and Y^{3+} is doped into the matrix to enhance the energy transfer from Gd^{3+} to Eu^{3+}. MTT assay showed a good biocompatibility of the NPs to cancer and normal cells and the cellular uptake was verified *via* inverted fluorescence microscopy after 48h incubation of BxPC-3 cells (human pancreatic cancer cells) with the NPs. As shown in Figure 33a, in which the nuclei of the cells are stained in blue with 4',6-diamidino-2-phenylindole (DAPI) the cytoplasmic region showed red fluorescence (upon excitation at 330-385 nm) due to the NPs, clearly demonstrating the possibility to use this material as fluorescent probe. At the same time, as shown in Figure 33b, a signal enhancement in the T_1-weigthed images and a signal decrease in the T_2-weighted images was observed at increasing concentration of Gd^{3+}, demonstrating that YGO-Bmnc can be efficient T_1 contrast agent and overall they can be used as a dual-function imaging probe for simultaneous MRI/OI.

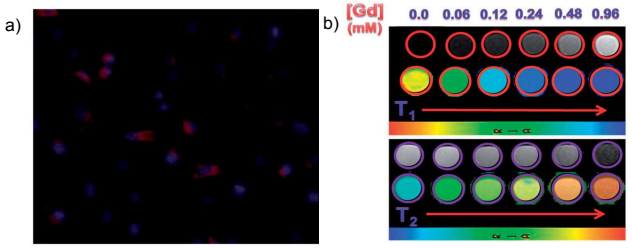

Figure 33 a) Inverted fluorescence microscopy images of BxPC-3 cells incubated with YGO-Bmnc NPs upon excitation at 330-385 nm; b) T_1 and T_2-weighted images and colour maps of YGO-Bmnc NPs at various Gd^{3+} concentration. Adapted with permission from J. Mat. Chem. B, 2014, 2265-2275. Copyright 2014 RSC.

A recent example of MRI/OI multimodal system has been reported by Mohapatra and collaborators.[212] The authors prepared hollow mesoporous silica nanoparticles incorporating iron oxide nanoparticles for MRI and carbon dots (CD) for OI and they also conjugated them with camptothecin (CPT, an anticancer drug) and folic acid for targeting, obtaining Fe_3O_4@m-SiO_2-CD-FA-CPT. The uptake of NPs *in vitro* was evaluated after incubation of HeLa cells. After 30 minutes a green fluorescence due to the CD was observed. MRI demonstrated that a magnetic contrast on the T_2 could be detected after 1h exposition.

Iron oxide as MRI probe in multimodal core/shell silica nanoparticles was proposed also by Jang and Lee.[213] A NIR-emitting cyanine, namely Cy5.5, was conjugated for *in vivo* imaging of squamous cell carcinoma (SCC7) xenografted mouse. The NPs chosen for the *in vivo* studies (CY-CS113) were PEGylated and their dimension was around 113 nm. As shown in Figure 34a the tumour area was significantly darkened in the T_2-weighted images. OI imaging was performed by exciting the sample at 670 nm and registering the emission at 700 nm. A strong fluorescent signal was detected in the tumour area as shown in Figure 34b. Interestingly, when NPs of 20 nm (CY-CS20) were injected, only a weak fluorescent signal was observed (Figure 34c) due to a quenching effect that the authors correlated to the distance between the dye and the surface of the nanoparticles.

.

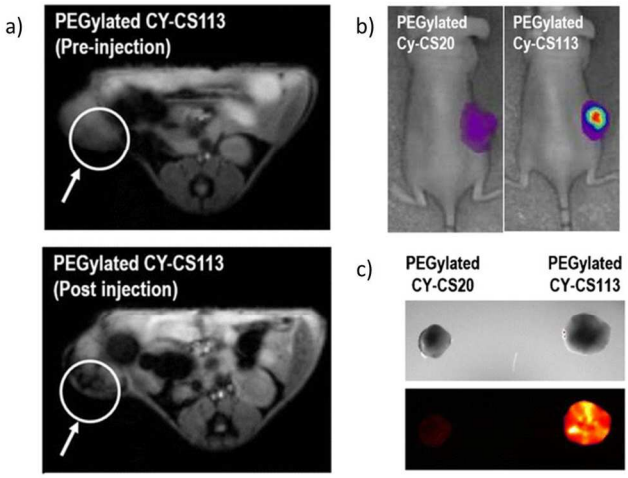

Figure 34 *In vivo* a) MRI and b) NIR fluorescence imaging of SCC7 xenografted mouse injected with PEGylated CY-CS113 (MRI) and PEGylated CY-CS113 and PEGylated CY-CS20 (NIR fluorescence imaging); c) NIR fluorescence imaging of excised tumour with PEGylated CY-CS113 and PEGylated CY-CS20. Adapted with permission from *Pharm. Res.*, 2014, doi 10.1007/s11095-014-1426-z. Copyright 2014 Springer.

A ^{19}F MR/fluorescent multimodal imaging agent has been proposed by Zhou and co-workers and it is based on fluorescein functionalized mesoporous silica nanoparticles (FMSNs) capping AuNP containing hexafluorobenzene as ^{19}F contrast agent and folic acid as targeting agent.[214] The conjugation of AuNPs onto FMSNs by acid-cleavable hydrazone linkage allows the release of the ^{19}F contrast agent only at pH<6.0 as schematically shown in Figure 35.

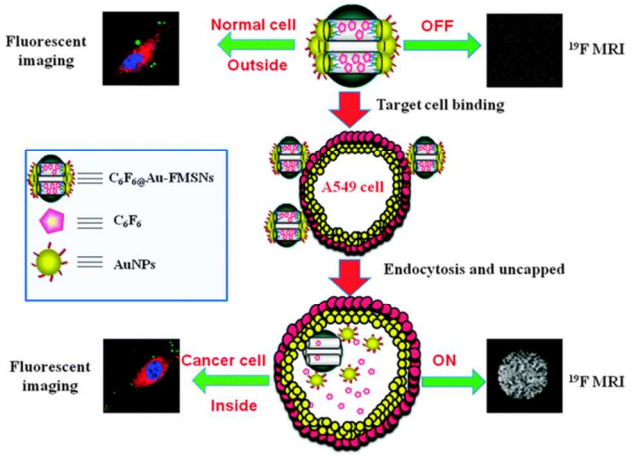

Figure 35 Scheme of the pH-triggered release of ^{19}F contrast agent from Au-FMSNs and MRI and OI response towards cancer and non-cancer cells. Adapted with permission from Chem. Commun., 2014, 50, 283-285. Copyright 2014 RSC.

The efficiency of the system was tested on human lung cancer cells (A549). Optical imaging allowed the localization of the NPs in the cytoplasmatic and nuclei regions after 3h of incubation while ^{19}F-MRI showed an increase in the contrast in cancer cells after 60 minutes of incubation. The release of the contrast agent was driven by the acidic extracellular pH of the tumour tissues. It was also demonstrated that the NPs were not internalized by normal human lung fibroblast cells.

MRI can also be combined, within the same nanoplatform, with US obtaining a diagnostic tool which can give three dimensional spatial resolution and permits real time monitoring.[215, 216] For this purpose superparamagnetic nanoparticles have been loaded on polymers or liposomes microcapsules.[176, 217, 218] However, clinical application of those systems is limited by their large micrometre size and high polydispersity as well as by the relatively low strength of the organic shells. Recently, Shi and co-workers have reported on multimodal hollow silica NPs containing manganese oxide nanoparticles highly dispersed in the silica matrix for MRI and high intensity focused ultrasound (HIFU).[193, 219]

Yang, Hu and co-workers have also reported on hollow silica nanospheres (HSNSs) that combine the possibility of performing MRI and US by conjugating Gd-DTPA on 400 nm size nanoparticles and targeting them with c(RGD), a peptide specific for $\alpha_v\beta_3$ integrin which express during angiogenesis.[220] The NPs (HSNSs@(DTPA-Gd)-RGD) were intravenously injected into PC3 (human prostate cancer) tumour-bearing mouse. As shown in Figure 36b the contrast in the tumour increased significantly. When MR imaging was performed the tumour site showed significant time-dependent brightness as demonstrated by the T_1-weighted images reported in Figures 36c-e.

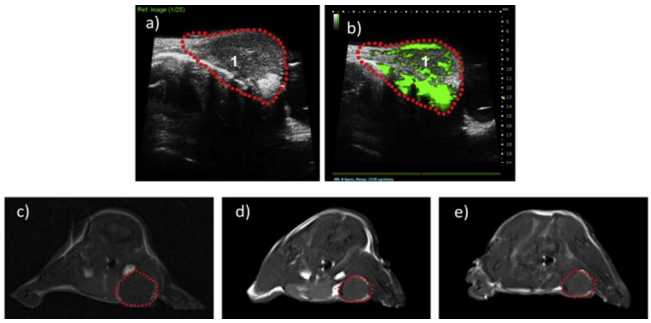

Figure 36 US images of PC3 tumour bearing mouse a) pre injection and b) post injection and T_1-weighted MRI images of PC3 tumour bearing mouse c) pre injection, d) after 1h e) after 4 h. Red circles point out the tumour region. Adapted with permission from Biomaterials, 2014, 35, 5381-5392. Copyright 2014 Elsevier.

The combination of OI and PET have also recently attracted the attention of scientists.[136, 221-224] Indeed, OI allows spatial visualization and high resolution as well as economic advantages, but it lacks in tissue penetration. PET, on the other hand, suffers from low spatial resolution but it is the most sensitive and specific technique for *in vivo* imaging. In particular Bradbury and co-workers have reported on OI/PET systems for sentinel lymph node and melanoma imaging.[18, 225, 226]

Very recently Cai and collaborators have described targeted mesoporous silica nanoparticles for PET/NIR imaging of tumour vasculature *in vivo*.[227] MSN were labelled with ^{64}Cu as PET tracer and 800CW as NIR fluorescent dye, and targeted with TRC105 (Fab) vascular targeting moiety. *In vivo* tumour targeted imaging was carried out in 4T1 murine breast tumour-bearing mice after injecting 5-10 MBq of ^{64}Cu-MSN-800CW-TR105(Fab) or non-radioactive labelled MSN-800CW-TR105(Fab) (~ 400 pmol of dye).The accumulation of ^{64}Cu-MSN-800CW-TR105(Fab) in 4T1 tumour was demonstrated by PET as shown in Figure 37a. When the same NPs were administrated injected in a mouse after administration of a blocking dose of free TRC105 a significantly reduced tumour uptake was observed. The *in vivo* NIR fluorescence imaging was measured 4h after injection of MSN-800CW-TR105(Fab), when the NPs showed the highest tumour accumulation based on PET imaging. The picture showed in Figure 37b demonstrates the effectiveness of the NPs proposed by Cai as OI probes.

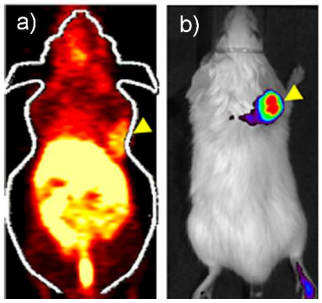

Figure 37 *In vivo* a) PET image and b) NIR fluorescence image of a 4T1 tumour bearing mice after 4h injection of ^{64}Cu-MSN-800CW-TR105(Fab) and MSN-800CW-TR105(Fab). Tumour is indicated by a yellow arrowhead. For NIR fluorescence λ_{exc} = 745 nm, λ_{em}. = 800 nm. Reproduced with permission from Mol Pharmaceutics, 2014, DOI 10.1021/mp500306k. Copyright 2014 ACS.

OI can also be coupled with CT. This strategy could be very useful in oncology as CT can help planning a surgery as provide location, shape and size of the tumours, while OI, and in particular fluorescence in the NIR region, can facilitate the identification of the tumour. An example of nanoparticles combining OI and CT was reported by Hayashi and collaborators.[228] The authors proposed PEGylated clustered gold nanoparticles-fluorescent silica core-shell nanoparticles (c-AuNPs@SiO_2 NPs) in which the fluorophore was a porphirine. When injected intravenously in tumour-bearing mice both CT and OI could be performed (see Figure 38). As shown in Figure 38C and D, 24h after the injection of the NPs, an increase in the contrast of the CT images was observed in the stomach and intestine areas filled with food that absorb X-rays (white arrows) and in the tumour area (black arrows). After 24h from injection OI (Figure 38F) showed an increase in the fluorescence of the tumour area. After 60h from injection the NPs were almost completely excreted.

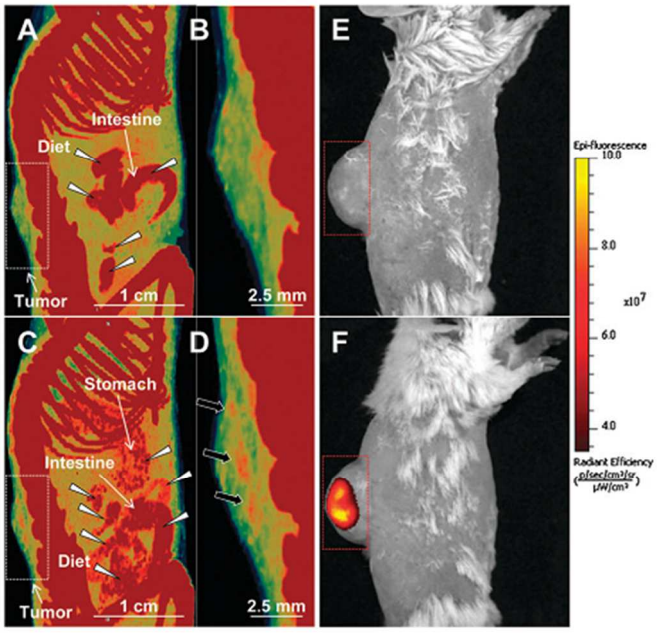

Figure 38 CT images (A-D) and *in vivo* fluorescence images (E-F) of tumour-bearing mouse injected intravenously with PEGylated c-AuNPs@SiO_2 NPs. A) and E) Pre-injection, B) zoom in the tumour area before the injection, C) after 24 h from injection, D) zoom in the tumour area 24h after injection, F) 24h after injection. Reproduced with permission from Chem. Commun., 2013, 39, 5334-5336. Copyright 2013, RSC.

The same authors reported also on near-infrared fluorescent (NIRF) silica-coated gold nanoparticle clusters for dual CT and optical imaging of lymphatic system.[229]

The possibility of combining more than two imaging techniques in the same nano object has also been explored. Zhang, Wang and collaborators have reported on lanthanide doped upconverting nanoparticles (UNPs) covalently conjugated on methylphosphonate functionalised silica nanospheres (pSiNPs) obtaining a system that can be used for *in vivo* upconversion luminescence, MRI and CT.[230] Also Shi and co-workers have described the combination of luminescence/MR/CT trimodal imagings by a novel multifunctional core/satellite nanotheranostic by decorating ultrasmall CuS nanoparticles onto the surface of a silica-coated rare-earth upconversion NPs.[203] The system proposed allowed simultaneously multimodal imaging and synergistic RT (radiotherapy) and PTA (photothermal ablation) therapy.

Therapy and Imaging

Following the recent advances in nanotechnology and prompted by the growing attention to nanochemistry,[15, 84, 231-242] nanomedicine can now benefit from a variety of new skills and develop more complex multi-functional materials for medical applications. For example, traditional nanocarriers developed for drug delivery purposes, which might experience unexpected drug release during circulation, can now be replaced by more complex nanomaterials, equipped with suitable gatekeepers able to lock the loaded drug into the pores and selectively release the cargo in response to an external stimulus.[16, 238, 242-245] Depending on the gatekeeper used, the activating stimuli can include variation in pH,[246-249] enzyme activation,[85, 250, 251] redox potential,[252] temperature,[253, 254] light,[255-257] and magnetic field.[258] In a recent paper Zink and co-workers[259] described a reversible and reusable system based on a-cyclodextrin nanovalves assembled on MSNs, capable to release the cargo under near-UV light irradiation and to reseal the pores when the light irradiation is turned off. In this way, it is possible to control the cargo release by simply modulating the light irradiation. Although most of the systems mentioned above were only applied *in vitro* due to the complexity of the *in vivo* environment,[260] however, such advances are promising for future applications in cancer therapy, where a selective release in the targeted cancer site, and, consequently, a decrease on the side effects of chemiotherapics is desirable.

The current approach in nanomedicine involves the combination of both diagnostic and therapeutic features integrated on the same platform.[261] In this regard silica-based nanoparticles, due to their intrinsic features as previously described and particularly for their facile surface functionalization, are suitable nanostructured matrixes for the development of multifunctional nanomedical platforms.[262] As described in previous sections, such silica-based nanoplatforms can be easily combined with a large variety of imaging techniques (single or multimodal). We report here a selection of recent examples simultaneously involving therapy and imaging techniques.

Jin and co-workers[263] have recently reported a carboxyl functionalized mesoporous silica nanoparticles (MSNs /COOH) nanocarrier loaded with doxorubicin (DOX) and modified with folate moiety and a NIRF dye, for anti-cancer drug delivery and bioimaging. Huang, Wang and colleagues[264] designed a FRET based mesoporous MSNs drug delivery system for *in vitro* imaging and monitoring of intracellular drug release. A similar approach was followed by Lu, Li et al.[265] which developed a hollow mesoporous silica based system for monitoring drug release in real time.

In some cases the intrinsic fluorescence of the nanocarriers can be directly applied for drug delivery and imaging.[266] Very recently Chen, Zhen et al.[267] developed and tested for both in *vitro* and *in vivo* applications, label-free luminescent MSNPs loaded with DOX.

In a recent paper, as already described in the PET section, Cai and co-workers[133] reported a multifunctional nanodevice consisting of functionalized mesoporous silica NPs for actively targeted PET imaging and drug delivery in 4T1 murine breast tumour-bearing mice. The MSNs matrix was functionalized with SH-PEG, TRC105 antibody (specific to CD105/endoglin) and Cu labelling for PET imaging. The system was also loaded with DOX and intravenously injected into 4T1 tumour-bearing mice and the distribution of the nanoparticles in the tumour tissue and in organs such as liver, heart and kidney was scanned (Figure 39) by *in vivo* imaging system, IVIS (λ_{exc} = 465 nm; λ_{em}

= 580 nm). The results showed selective delivery of the anticancer drug into the tumour site and highlight the potential application of this system for image-guided drug delivery and targeted cancer therapy.

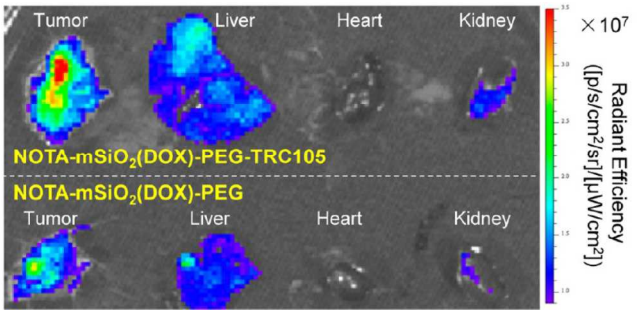

Figure 39 An *ex vivo* optical image of major organs at 0.5h after intravenous injection of NOTA-mSiO$_2$(DOX)-PEG-TRC105 in 4T1 tumour-bearing mice, which clearly showed stronger tumour DOX signal in the former. Adapted with permission from *ACS Nano*, 2013, *7*, 9027–9039. Copyright 2013, *ACS*.

Anker and co-workers[268] recently reported a magnetic nanocapsule based on iron nanocore and a mesoporous silica shell for MRI imaging, magnetically assisted drug delivery and controlled drug release.

Shi, Chen and co-workers[269] developed a general procedure to prepare manganese oxide/MSNs-based nanoparticles for *in vitro* and *in vivo* T_1-MRI imaging and drug delivery. The nanodevice was obtained by dispersing manganese oxide within mesopore channels of MSNs. The system proved both *in vitro* and *in vivo* a high performance for T_1-MRI. Furthermore, the drug delivery capability and the intracellular release by a pH-responsive mechanism were confirmed. In a more recent paper Shi's and Li's groups[270] proposed a further multifunctional nanodevice based on ultrasmall iron oxide nanoparticles dispersed within mesopore channels of MSNs for highly efficient T_1-weighted MRI and pH-stimuli-responsive drug delivery. The iron oxide MSNs were loaded with DOX and intratumorally injected in mice bearing tumour showing an increase of the *in vivo* T_1-MRI signals at the tumour site (Figure 40).

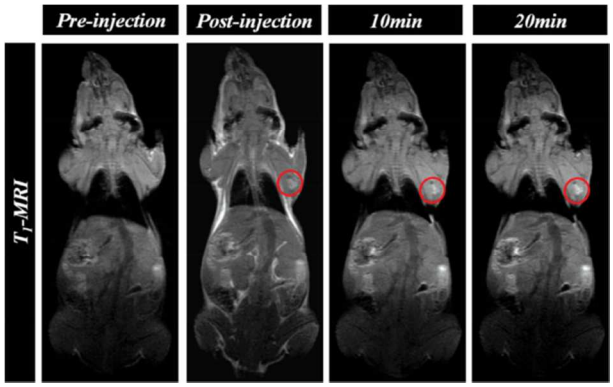

Figure 40 *In vivo* T_1 -MRI of a tumour-bearing mouse before and after the injection of DOX-Fe-MSNs for varied time durations. Adapted with permission from Adv. Funct. Mater., 2014, 24, 4273–4283. Copyright 2014, Wiley-VCH.

The availability of multimodal imaging probes can be exploited to develop more complex multifunctional systems.

A MRI/OI multimodal nanodevice for imaging and drug delivery was proposed by Nel, Tamanoi, Zink *et al.*[204] which encapsulated superparamagnetic iron oxide nanocrystals into mesostructured silica spheres. The system was also labelled with fluorescein and targeted with folic acid to increase the cellular uptake. The NPs were loaded with water-insoluble anticancer drugs such as camptothecin (CPT) and paclitaxel (TXL) and their efficacy was tested *in vitro* on pancreatic cancer cell lines PANC-1 and BxPC3. A further example of multifunctional platform for drug delivery and MRI/OI imaging was reported by Hyeon's group[205] and consists of a versatile nanodevice synthesised by decorating a mesoporous dye-doped silica matrix with magnetite nanocrystals. Mohapatra and co-workers[212] provided a further and more recent example of MRI/OI imaging applied to drug delivery. The system consists of magnetic mesoporous spherical particles with fluorescent carbon encapsulated within the mesoporous framework. The system was loaded with CPT and targeted with folic acid.

Bu, Shi *et al.*[206] developed a multimodal system based on $NaYF_4$:Yb/Tm@$NaGdF_4$ core/hollow mesoporous silica shell nanoparticles for NIR-triggered drug delivery and *in situ* quantitative drug release monitoring by both upconverted luminescence (UCL) and T_1-MRI in real time.

In a recent article Chen, Hong and co-workers[207] combined PET/NIRF into hollow mesoporous silica nanoparticles (HMSNs) for *in vivo* imaging and targeted drug delivery. This system is very similar to that described in the multimodal section.[227] The HMSNs substrate was conjugated with a NIR dye (ZW800), a targeting agent (TRC105), and the PET isotope ^{64}Cu to form the multifunctional HMSN based ^{64}Cu-HMSN-ZW800-TRC105. *In vivo* tumour targeted PET and NIRF imaging were carried out in 4T1 murine breast tumour-bearing mice (Figures 41a and 41b). The *in vivo* tumour targeted drug delivery was also evaluated by loading the system with DOX and injecting the HMSN(DOX)-TRC105 in 4T1 tumour-bearing mice (HMSN dose: 10 mg/kg, DOX dose: 6.5 mg/kg) and images in the IVIS system (λ_{exc} = 465 nm; λ_{em} = 580 nm) of the major organs collected to detect the presence of DOX in presence and in absence of the targeting agent (Figure 41c).

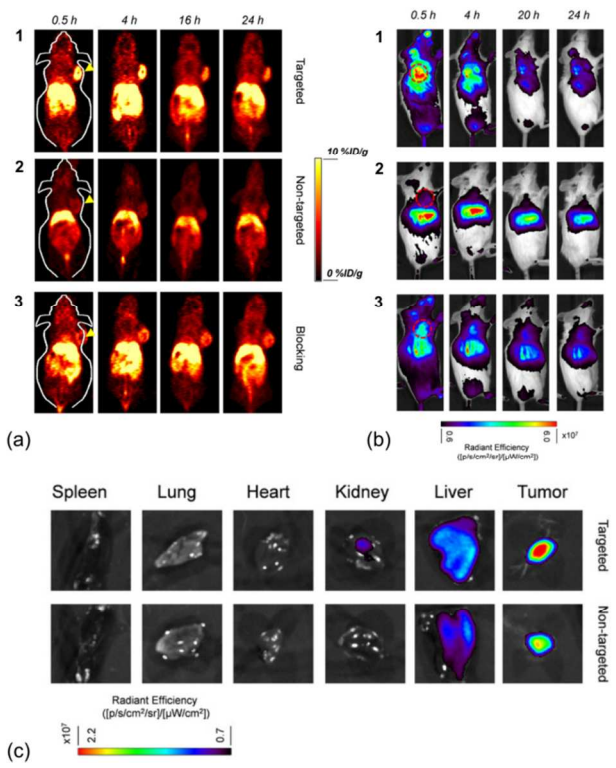

Figure 41 (a) *In vivo* tumour targeted PET imaging. Serial coronal PET images of 4T1 tumour-bearing mice at different time points post-injection. (1) targeted group: ^{64}Cu-HMSN-ZW800-TRC105, (2) non-targeted group: ^{64}Cu-HMSN-ZW800, or (3) blocking group: ^{64}Cu-HMSN-ZW800-TRC105 with a blocking dose (1 mg/mouse) of free TRC105. (b) *In vivo* tumour targeted NIRF imaging. In both example (1) Targeted group. (2) Non-targeted group. (3) Blocking group. Tumours were marked by dashed red circles. (c) *Ex vivo* optical imaging of major organs after i.v. injection of HMSN(DOX)-(w/o)-TRC105 in 4T1 tumour-bearing mice. HMSN dose was 10 mg/kg, while the DOX dose was 6.5 mg/kg (Ex = 465 nm, Em = 580 nm). Adapted with permission from Sci. Rep., 2014, DOI: 10.1038/srep05080. Copyright 2014, Nature.

Alternative therapeutic approaches might involve photothermal therapy (PTT), radiotherapy (RT) photo dynamic therapy (PDT) and/or a combination of these therapeutic modes with chemotherapy.[115, 162, 203, 208, 271-277]

In 2012 Chen, Shi and co-workers[272] reported and characterised a versatile multifunctional nanodevice which integrates chemotherapy, photo-thermotherapy, *in vivo* MRI, and infrared thermal imaging consisting of well-dispersed gold nanorods-capped magnetic core/mesoporous silica shell nanoellipsoids (Au NRs-MMSNEs).

In the same year Chen, Wu and colleagues[277] developed mesoporous silica-coated gold nanorods for *in vitro* two-photon imaging (TPI) and therapy. The system was loaded with the anticancer drug DOX and released by the application of low intensity NIR laser irradiation, working as light activated drug delivery system. Furthermore, the use of NIR laser irradiation at higher intensity induced hyperthermia effects of the AuNRs, providing a further therapeutic mode.

As already described in the CT section, Cui *et al.*[162] synthesised folic acid conjugated silica modified gold nanorods (GNR-SiO_2-FA) as multifunctional nanodevice for dual-mode radiation therapy (RT)-photothermal therapy (PTT), *in vivo* CT imaging for MGC803 gastric cancer cells. The *in vitro* investigation showed enhanced RT effects, and excellent PTT effects on MGC803 gastric cancer cells. The *in vivo* study highlighted the potential of this system in tumour targeting and CT imaging, making this multifunctional nanodevice a good candidate for *in vivo* targeting dual-mode therapy and future applications in clinical patients with tumour cancer. In a recent paper Shi, Bu *et al.*[203] described the development of a multifunctional core/satellite nanotheranostic (CSNT) combining photothermal ablation (PTA), radiotherapy (RT) and UPL/MR/CT trimodal imaging. The system consists of silica-coated rare-earth upconversion nanoparticles (the core), decorated with ultrasmall CuS nanoparticles (the satellite). The core provides the UPL/MR/CT trimodal imaging and, at the same time, acts as radiosensitizer determining an increase of the radiation dose of RT. The satellite acts as photothermal agents to increase photothermal conversion efficacy. *In vitro* and *in vivo* studies suggested a synergistic effect between RT and PTA and confirmed the applicability of this system for UCL/MR/CT trimodal imaging.

Wang and co-workers[115] have developed methylene blue encapsulated phosphonate-terminated silica nanoparticles which simultaneously combine real time *in vivo* NIR optical imaging (see Optical Imaging section) and Photo Dynamic Therapy PDT. The system was intratumorally injected in mice bearing HeLA tumour inducing a damage in tumour tissues and consequently a reduction of the tumour mass (Figure 42). At the same time the fluorescence emission of the MB in the silica NPs allowed an *in vivo* tumour imaging.

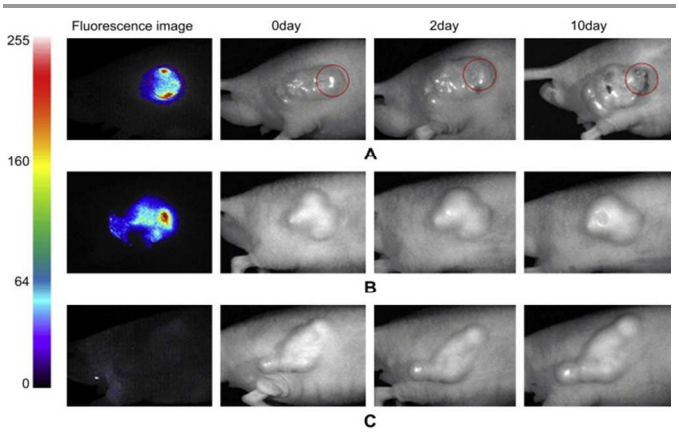

Figure 42 *In vivo* imaging and PDT of subcutaneous-Hela-tumour-xenografted mice after different treatment: (A) 100 ml 44 mg/ml MB-encapsulated phosphonate-terminated silica nanoparticles injection and 5 min light exposure with power intensity of 500 mw/cm^2, the red circle indicates the region injected the MB-encapsulated PSiNPs and with light exposure; (B) 100 ml 44 mg/ml MB-encapsulated PSiNPs injection; and (C) 5 min light exposure with power intensity of 500 mw/cm^2. Reproduced with permission from Biomaterials 2009, 30, 5601-5609. Copyright 2009, Elsevier.

A further MB-based system was recently reported by Jang and co-workers. These authors developed methylene blue-loaded gold nanorod@SiO_2 nanoparticles for cancer imaging and photothermal/photodynamic dual therapy.[273]

Chen, Zheng *et al.* [208] developed multimodal core-shell-structured MSNs which combine MRI, fluorescence imaging and PDT. The

system was targeted with folic acid, increasing the selectivity to cancer cells and was reported to minimise the damage of normal tissues due to the PDT.

Conclusions

In conclusion, the chosen examples demonstrate that silica-based nanoparticles are a versatile tool for the development of efficient bioimaging agents, for both *in vitro* and *in vivo* applications. As discussed in the last session, they can also be used as multifunctional nanoplatforms for both diagnostic and therapeutic purposes for the development of personalised healthcare. However, it is surprising that, despite the vast amount of examples described in the literature, still silica-based nanoparticles are only in a preclinical development stage. Although the road has already been traced, however further advancements needs to be achieved before nanomedicine could become an everyday clinical practice and a lot of effort should be devoted to translational research in the future. Chemists, in close collaboration with biologists and physicians, will play a key role to accomplish this fundamental social challenge.

Acknowledgements

We would like to thank Regione Autonoma della Sardegna (CRP-59699) for financial support.

Notes and references

[a]*Università degli Studi di Cagliari, Dipartimento di Scienze Chimiche e Geologiche, S.S. 554 bivio per Sestu, 09042 Monserrato (CA), ITALY. e-mail: ccaltagirone@unica.it; Fax: +39 070 675 4456; Tel:+ 39 070 675 4452*

1. K. Riehemann, S. W. Schneider, T. A. Luger, B. Godin, M. Ferrari and H. Fuchs, *Angew. Chem., Int. Ed.*, 2009, **48**, 872-897.
2. E. C. Cho, C. Glaus, J. Chen, M. J. Welch and Y. Xia, *Trends Mol. Med.*, 2010, **16**, 561-573.
3. H. S. Choi and J. V. Frangioni, *Mol. Imaging*, 2010, **9**, 291-310.
4. J. L. Vivero-Escoto, R. C. Huxford-Phillips and W. Lin, *Chem. Soc. Rev.*, 2012, **41**, 2673-2685.
5. S. Achilefu, *Chem. Rev.*, 2010, **110**, 2575-2578.
6. X. Gao, Y. Cui, R. M. Levenson, L. W. K. Chung and S. Nie, *Nat. Biotechnol.*, 2004, **22**, 969-976.
7. I. L. Medintz, H. T. Uyeda, E. R. Goldman and H. Mattoussi, *Nat. Mater.*, 2005, **4**, 435-446.
8. X. Michalet, F. F. Pinaud, L. A. Bentolila, J. M. Tsay, S. Doose, J. J. Li, G. Sundaresan, A. M. Wu, S. S. Gambhir and S. Weiss, *Science*, 2005, **307**, 538-544.
9. R. R. Arvizo, S. Bhattacharyya, R. A. Kudgus, K. Giri, R. Bhattacharya and P. Mukherjee, *Chem. Soc. Rev.*, 2012, **41**, 2943-2970.
10. S. E. Skrabalak, J. Chen, Y. Sun, X. Lu, L. Au, C. M. Cobley and Y. Xia, *Acc. Chem. Res.*, 2008, **41**, 1587-1595.
11. S. Laurent, D. Forge, M. Port, A. Roch, C. Robic, L. Vander Elst and R. N. Muller, *Chem. Rev.*, 2008, **108**, 2064-2110.
12. S. Mornet, S. Vasseur, F. Grasset and E. Duguet, *J. Mater. Chem.*, 2004, **14**, 2161-2175.
13. Y. Chen, H. Chen and J. Shi, *Adv. Mater. (Weinheim, Ger.)*, 2013, **25**, 3144-3176.
14. *http://www.accessdata.fda.gov/scripts/fdcc/?set=GRASNotices&sort=GRN_No&order=DESC&startrow=1&type=basic&search=silica*.
15. W. Arap, R. Pasqualini, M. Montalti, L. Petrizza, L. Prodi, E. Rampazzo, N. Zaccheroni and S. Marchió, *Curr. Med. Chem.*, 2013, **20**, 2195-2211.
16. M. W. Ambrogio, C. R. Thomas, Y. L. Zhao, J. I. Zink and J. F. Stoddart, *Acc. Chem. Res.*, 2011, **44**, 903-913.
17. J. M. Rosenholm, C. Sahlgren and M. Lindén, *Nanoscale*, 2010, **2**, 1870-1883.
18. M. Benezra, O. Penate-Medina, P. B. Zanzonico, D. Schaer, H. Ow, A. Burns, E. DeStanchina, V. Longo, E. Herz, S. Iyer, J. Wolchok, S. M. Larson, U. Wiesner and M. S. Bradbury, *J. Clin. Invest.*, 2011, **121**, 2768-2780.
19. W. Stöber, A. Fink and E. Bohn, *J. Colloid Interface Sci.*, 1968, **26**, 62-69.
20. R. P. Bagwe, C. Yang, L. R. Hilliard and W. Tan, *Langmuir*, 2004, **20**, 8336-8342.
21. Q. Huo, J. Liu, L. Q. Wang, Y. Jiang, T. N. Lambert and E. Fang, *J. Am. Chem. Soc.*, 2006, **128**, 6447-6453.
22. I. I. Slowing, J. L. Vivero-Escoto, B. G. Trewyn and V. S. Y. Lin, *J. Mater. Chem.*, 2010, **20**, 7924-7937.
23. Z. Cheng, A. Al Zaki, J. Z. Hui, V. R. Muzykantov and A. Tsourkas, *Science*, 2012, **338**, 903-910.
24. J. Fang, H. Nakamura and H. Maeda, *Adv. Drug Delivery Rev.*, 2011, **63**, 136-151.
25. D. Peer, J. M. Karp, S. Hong, O. C. Farokhzad, R. Margalit and R. Langer, *Nat. Nanotechnol.*, 2007, **2**, 751-760.
26. E. Ruoslahti, S. N. Bhatia and M. J. Sailor, *J. Cell Biol.*, 2010, **188**, 759-768.
27. G. M. Whitesides, *Nat. Biotechnol.*, 2003, **21**, 1161-1165.
28. P. Sharma, S. Brown, G. Walter, S. Santra and B. Moudgil, *Adv. Colloid Interface Sci.*, 2006, **123-126**, 471-485.
29. A. J. L. Villaraza, A. Bumb and M. W. Brechbiel, *Chem. Rev.*, 2010, **110**, 2921-2959.
30. S. Viswanathan, Z. Kovacs, K. N. Green, S. J. Ratnakar and A. D. Sherry, *Chem. Rev.*, 2010, **110**, 2960-3018.
31. A. Accardo, D. Tesauro, L. Aloj, C. Pedone and G. Morelli, *Coord. Chem. Rev.*, 2009, **253**, 2193-2213.
32. S. Aime, M. Botta and E. Terreno, in *Adv. Inorg. Chem.*, 2006, vol. 57, pp. 173-237.
33. S. Aime, S. G. Crich, E. Gianolio, G. B. Giovenzana, L. Tei and E. Terreno, *Coord. Chem. Rev.*, 2006, **250**, 1562-1579.
34. M. Bottrill, L. Kwok and N. J. Long, *Chem. Soc. Rev.*, 2006, **35**, 557-571.
35. P. Caravan, *Chem. Soc. Rev.*, 2006, **35**, 512-523.
36. K. W. Y. Chan and W. T. Wong, *Coord. Chem. Rev.*, 2007, **251**, 2428-2451.
37. G. L. Davies, I. Kramberger and J. J. Davis, *Chem. Commun.*, 2013, **49**, 9704-9721.
38. B. Drahoš, I. Lukeš and É. Tóth, *Eur. J. Inorg. Chem.*, 2012, 1975-1986.
39. M. C. Heffern, L. M. Matosziuk and T. J. Meade, *Chem. Rev.*, 2014, **114**, 4496-4539.

40. M. Kueny-Stotz, A. Garofalo and D. Felder-Flesch, *Eur. J. Inorg. Chem.*, 2012, 1987-2005.
41. S. Laurent, C. Henoumont, L. Vander Elst and R. N. Muller, *Eur. J. Inorg. Chem.*, 2012, 1889-1915.
42. D. Pan, A. H. Schmieder, S. A. Wickline and G. M. Lanza, *Tetrahedron*, 2011, **67**, 8431-8444.
43. E. Terreno, D. D. Castelli, A. Viale and S. Aime, *Chem. Rev.*, 2010, **110**, 3019-3042.
44. J. A. Peters and K. Djanashvili, *Eur. J. Inorg. Chem.*, 2012, 1961-1974.
45. M. Botta and L. Tei, *Eur. J. Inorg. Chem.*, 2012, 1945-1960.
46. K. M. L. Taylor, J. S. Kim, W. J. Rieter, H. An, W. Lin and W. Lin, *J. Am. Chem. Soc.*, 2008, **130**, 2154-2155.
47. W. J. Rieter, J. S. Kim, K. M. L. Taylor, H. An, W. Lin, T. Tarrant and W. Lin, *Angew. Chem., Int. Ed.*, 2007, **46**, 3680-3682.
48. J. K. Hsiao, C. P. Tsai, T. H. Chung, Y. Hung, M. Yao, H. M. Liu, C. Y. Mou, C. S. Yang, Y. C. Chen and D. M. Huang, *Small*, 2008, **4**, 1445-1452.
49. N. Wartenberg, P. Fries, O. Raccurt, A. Guillermo, D. Imbert and M. Mazzanti, *Chem.-Eur. J.*, 2013, **19**, 6980-6983.
50. F. Carniato, L. Tei, A. Arrais, L. Marchese and M. Botta, *Chem.-Eur. J.*, 2013, **19**, 1421-1428.
51. V. Feldmann, J. Engelmann, S. Gottschalk and H. A. Mayer, *J. Colloid Interface Sci.*, 2012, **366**, 70-79.
52. S. L. C. Pinho, H. Faneca, C. F. G. C. Geraldes, M. H. Delville, L. D. Carlos and J. Rocha, *Biomaterials*, 2012, **33**, 925-935.
53. S. Santra, R. P. Bagwe, D. Dutta, J. T. Stanley, G. A. Walter, W. Tan, B. M. Moudgil and R. A. Mericle, *Adv. Mater. (Weinheim, Ger.)*, 2005, **17**, 2165-2169.
54. C. Wu, J. Hong, X. Guo, C. Huang, J. Lai, J. Zheng, J. Chen, X. Mu and Y. Zhao, *Chem. Commun.*, 2008, 750-752.
55. S. L. C. Pinho, H. Faneca, C. F. G. C. Geraldes, J. Rocha, L. D. Carlos and M. H. Delville, *Eur. J. Inorg. Chem.*, 2012, 2828-2837.
56. W. P. Cacheris, S. C. Quay and S. M. Rocklage, *Magnetic Resonance Imaging*, 1990, **8**, 467-481.
57. Y. Z. Shao, L. Z. Liu, S. Q. Song, R. H. Cao, H. Liu, C. Y. Cui, X. Li, M. J. Bie and L. Li, *Contrast Media and Molecular Imaging*, 2011, **6**, 110-118.
58. Y. Shao, X. Tian, W. Hu, Y. Zhang, H. Liu, H. He, Y. Shen, F. Xie and L. Li, *Biomaterials*, 2012, **33**, 6438-6446.
59. C. C. Huang, C. Y. Tsai, H. S. Sheu, K. Y. Chuang, C. H. Su, U. S. Jeng, F. Y. Cheng, C. H. Su, H. Y. Lei and C. S. Yeh, *ACS Nano*, 2011, **5**, 3905-3916.
60. J. W. M. Bulte and D. L. Kraitchman, *NMR Biomed.*, 2004, **17**, 484-499.
61. S. H. Wu, Y. S. Lin, Y. Hung, Y. H. Chou, Y. H. Hsu, C. Chang and C. Y. Mou, *ChemBioChem*, 2008, **9**, 53-57.
62. Y. S. Lin, S. H. Wu, Y. Hung, Y. H. Chou, C. Chang, M. L. Lin, C. P. Tsai and C. Y. Mou, *Chem. Mater.*, 2006, **18**, 5170-5172.
63. H. M. Liu, S. H. Wu, C. W. Lu, M. Yao, J. K. Hsiao, Y. Hung, Y. S. Lin, C. Y. Mou, C. S. Yang, D. M. Huang and Y. C. Chen, *Small*, 2008, **4**, 619-626.
64. J. Kim, H. S. Kim, N. Lee, T. Kim, H. Kim, T. Yu, I. C. Song, W. K. Moon and T. Hyeon, *Angew. Chem., Int. Ed.*, 2008, **47**, 8438-8441.
65. H. Wu, G. Liu, S. Zhang, J. Shi, L. Zhang, Y. Chen, F. Chen and H. Chen, *J. Mater. Chem.*, 2011, **21**, 3037-3045.
66. L. Zhang, Y. Wang, Y. Tang, Z. Jiao, C. Xie, H. Zhang, P. Gu, X. Wei, G. Y. Yang, H. Gu and C. Zhang, *Nanoscale*, 2013, **5**, 4506-4516.
67. A. A. Gilad, P. Walczak, M. T. McMahon, B. N. Hyon, H. L. Jung, K. An, T. Hyeon, P. C. M. Van Zijl and J. W. M. Bulte, *Magnetic Resonance in Medicine*, 2008, **60**, 1-7.
68. H. B. Na, J. H. Lee, K. An, Y. I. Park, M. Park, I. S. Lee, D. H. Nam, S. T. Kim, S. H. Kim, S. W. Kim, K. H. Lim, K. S. Kim, S. O. Kim and T. Hyeon, *Angew. Chem., Int. Ed.*, 2007, **46**, 5397-5401.
69. T. Kim, E. Momin, J. Choi, K. Yuan, H. Zaidi, J. Kim, M. Park, N. Lee, M. T. McMahon, A. Quinones-Hinojosa, J. W. M. Bulte, T. Hyeon and A. A. Gilad, *J. Am. Chem. Soc.*, 2011, **133**, 2955-2961.
70. H. Hu, A. Dai, J. Sun, X. Li, F. Gao, L. Wu, Y. Fang, H. Yang, L. An, H. Wu and S. Yang, *Nanoscale*, 2013, **5**, 10447-10454.
71. S. M. Kim, G. H. Im, D. G. Lee, J. H. Lee, W. J. Lee and I. S. Lee, *Biomaterials*, 2013, **34**, 8941-8948.
72. S. Mizukami, R. Takikawa, F. Sugihara, Y. Hori, H. Tochio, M. Wälchli, M. Shirakawa and K. Kikuchi, *J. Am. Chem. Soc.*, 2008, **130**, 794-795.
73. Y. Takaoka, T. Sakamoto, S. Tsukiji, M. Narazaki, T. Matsuda, H. Tochio, M. Shirakawa and I. Hamachi, *Nature Chem.*, 2009, **1**, 557-561.
74. J. Liu and L. S. Lee, *Environ. Sci. Technol.*, 2007, **41**, 5357-5362.
75. K. Tanaka, N. Kitamura, K. Naka and Y. Chujo, *Chem. Commun.*, 2008, 6176-6178.
76. H. Matsushita, S. Mizukami, F. Sugihara, Y. Nakanishi, Y. Yoshioka and K. Kikuchi, *Angew. Chem., Int. Ed.*, 2014, **53**, 1008-1011.
77. C. Kim, C. Favazza and L. V. Wang, *Chem. Rev.*, 2010, **110**, 2756-2782.
78. H. Kobayashi, M. Ogawa, R. Alford, P. L. Choyke and Y. Urano, *Chem. Rev.*, 2010, **110**, 2620-2640.
79. V. Ntziachristos, J. Ripoll, L. V. Wang and R. Weissleder, *Nat. Biotechnol.*, 2005, **23**, 313-320.
80. S. Das, A. M. Powe, G. A. Baker, B. Valle, B. El-Zahab, H. O. Sintim, M. Lowry, S. O. Fakayode, M. E. McCarroll, G. Patonay, M. Li, R. M. Strongin, M. L. Geng and I. M. Warner, *Anal. Chem.*, 2012, **84**, 597-625.
81. Z. B. Li, W. Cai and X. Chen, *J. Nanosci. Nanotechnol.*, 2007, **7**, 2567-2581.
82. Z. Cai, Z. Ye, X. Yang, Y. Chang, H. Wang, Y. Liu and A. Cao, *Nanoscale*, 2011, **3**, 1974-1976.
83. X. He, L. Hai, J. Su, K. Wang and X. Wu, *Nanoscale*, 2011, **3**, 2936-2942.
84. M. Montalti, L. Prodi, E. Rampazzo and N. Zaccheroni, *Chem. Soc. Rev.*, 2014, **43**, 4243-4268.
85. K. Patel, S. Angelos, W. R. Dichtel, A. Coskun, Y. W. Yang, J. I. Zink and J. F. Stoddart, *J. Am. Chem. Soc.*, 2008, **130**, 2382-2383.
86. A. Popat, S. B. Hartono, F. Stahr, J. Liu, S. Z. Qiao and G. Q. Lu, *Nanoscale*, 2011, **3**, 2801-2818.
87. A. Burns, H. Ow and U. Wiesner, *Chem. Soc. Rev.*, 2006, **35**, 1028-1042.
88. U. A. Gunasekera, Q. A. Pankhurst and M. Douek, *Targeted Oncology*, 2009, **4**, 169-181.
89. K. E. Sapsford, W. R. Algar, L. Berti, K. B. Gemmill, B. J. Casey, E. Oh, M. H. Stewart and I. L. Medintz, *Chem. Rev.*, 2013, **113**, 1904-2074.

90. L. Wang, K. Wang, S. Santra, X. Zhao, L. R. Hilliard, J. E. Smith, Y. Wu and W. Tan, *Anal. Chem.*, 2006, **78**, 646-654.
91. L. Wang, W. Zhao and W. Tan, *Nano Res.*, 2008, **1**, 99-115.
92. K. T. Yong, I. Roy, M. T. Swihart and P. N. Prasad, *J. Mater. Chem.*, 2009, **19**, 4655-4672.
93. X. He, J. Duan, K. Wang, W. Tan, X. Lin and C. He, *J. Nanosci. Nanotechnol.*, 2004, **4**, 585-589.
94. X. He, K. Wang, W. Tan, J. Li, X. Yang, S. Huang, D. Li and D. Xiao, *J. Nanosci. Nanotechnol.*, 2002, **2**, 317-320.
95. D. Liu, X. He, K. Wang, C. He, H. Shi and L. Jian, *Bioconjugate Chem.*, 2010, **21**, 1673-1684.
96. J. Peng, K. Wang, W. Tan, X. He, C. He, P. Wu and F. Liu, *Talanta*, 2007, **71**, 833-840.
97. K. Wang, X. He, X. Yang and H. Shi, *Acc. Chem. Res.*, 2013, **46**, 1367-1376.
98. P. Wu, X. He, K. Wang, W. Tan, D. Ma, W. Yang and C. He, *J. Nanosci. Nanotechnol.*, 2008, **8**, 2483-2487.
99. X. Xing, X. He, J. Peng, K. Wang and W. Tan, *J. Nanosci. Nanotechnol.*, 2005, **5**, 1688-1693.
100. L. Tao, K. Zhang, Y. Sun, B. Jin, Z. Zhang and K. Yang, *Biosensors and Bioelectronics*, 2012, **35**, 186-192.
101. R. Kumar, I. Roy, T. Y. Ohulchanskyy, L. N. Goswami, A. C. Bonoiu, E. J. Bergey, K. M. Tramposch, A. Maitra and P. N. Prasad, *ACS Nano*, 2008, **2**, 449-456.
102. H. Yang, C. Lou, M. Xu, C. Wu, H. Miyoshi and Y. Liu, *International journal of nanomedicine*, 2011, **6**, 2023-2032.
103. F. Cao, R. Deng, D. Liu, S. Song, S. Wang, S. Su and H. Zhang, *Dalton Trans.*, 2011, **40**, 4800-4802.
104. Z. Bai, R. Chen, P. Si, Y. Huang, H. Sun and D. H. Kim, *ACS Appl. Mater. Interfaces*, 2013, **5**, 5856-5860.
105. B. Korzeniowska, R. Nooney, D. Wencel and C. McDonagh, *Nanotechnology*, 2013, **24**.
106. Y. P. Chen, H. A. Chen, Y. Hung, F. C. Chien, P. Chen and C. Y. Mou, *RSC Advances*, 2012, **2**, 968-973.
107. X. Yu, X. Jia, X. Yang, W. Liu and W. Qin, *RSC Advances*, 2014, **4**, 23571-23579.
108. C. Zong, K. Ai, G. Zhang, H. Li and L. Lu, *Anal. Chem.*, 2011, **83**, 3126-3132.
109. Y. Shi, Z. Chen, X. Cheng, Y. Pan, H. Zhang, Z. Zhang, C. W. Li and C. Yi, *Biosensors and Bioelectronics*, 2014, **61**, 397-403.
110. S. K. Rastogi, P. Pal, D. E. Aston, T. E. Bitterwolf and A. L. Branen, *ACS Appl. Mater. Interfaces*, 2011, **3**, 1731-1739.
111. J. Peng, X. He, K. Wang, W. Tan, Y. Wang and Y. Liu, *Anal. Bioanal. Chem.*, 2007, **388**, 645-654.
112. X. Zhang, X. Zhang, B. Yang, L. Liu, J. Hui, M. Liu, Y. Chen and Y. Wei, *RSC Advances*, 2014, **4**, 10060-10066.
113. M. Soster, R. Juris, S. Bonacchi, D. Genovese, M. Montalti, E. Rampazzo, N. Zaccheroni, P. Garagnani, F. Bussolino, L. Prodi and S. Marchiò, *International Journal of Nanomedicine*, 2012, **7**, 4797-4807.
114. X. Chen, M. C. Estévez, Z. Zhu, Y. F. Huang, Y. Chen, L. Wang and W. Tan, *Anal. Chem.*, 2009, **81**, 7009-7014.
115. X. He, X. Wu, K. Wang, B. Shi and L. Hai, *Biomaterials*, 2009, **30**, 5601-5609.
116. X. He, Y. Wang, K. Wang, M. Chen and S. Chen, *Anal. Chem.*, 2012, **84**, 9056-9064.
117. E. Rampazzo, S. Bonacchi, D. Genovese, R. Juris, M. Montalti, V. Paterlini, N. Zaccheroni, C. Dumas-Verdes, G. Clavier, R. Méallet-Renault and L. Prodi, *J. Phys. Chem. C*, 2014, **118**, 9261-9267.
118. E. Rampazzo, F. Boschi, S. Bonacchi, R. Juris, M. Montalti, N. Zaccheroni, L. Prodi, L. Calderan, B. Rossi, S. Becchi and A. Sbarbati, *Nanoscale*, 2012, **4**, 824-830.
119. M. Helle, E. Rampazzo, M. Monchanin, F. Marchal, F. Guillemin, S. Bonacchi, F. Salis, L. Prodi and L. Bezdetnaya, *ACS Nano*, 2013, **7**, 8645-8657.
120. X. Wang, A. R. Morales, T. Urakami, L. Zhang, M. V. Bondar, M. Komatsu and K. D. Belfield, *Bioconjugate Chem.*, 2011, **22**, 1438-1450.
121. S. Gandhi, K. Thandavan, B. J. Kwon, H. J. Woo, S. S. Yi, H. S. Lee, J. H. Jeong, K. Jang and D. S. Shin, *RSC Advances*, 2014, **4**, 5953-5962.
122. C. H. Lee, S. H. Cheng, Y. J. Wang, Y. C. Chen, N. T. Chen, J. Souris, C. T. Chen, C. Y. Mou, C. S. Yang and L. W. Lo, *Adv. Funct. Mater.*, 2009, **19**, 215-222.
123. K. Ma, H. Sai and U. Wiesner, *J. Am. Chem. Soc.*, 2012, **134**, 13180-13183.
124. S. Palantavida, R. Tang, G. P. Sudlow, W. J. Akers, S. Achilefu and I. Sokolov, *Journal of Materials Chemistry B*, 2014, **2**, 3107-3114.
125. L. Tao, C. Song, Y. Sun, X. Li, Y. Li, B. Jin, Z. Zhang and K. Yang, *Anal. Chim. Acta*, 2013, **761**, 194-200.
126. X. Yang, Z. Li, M. Li, J. Ren and X. Qu, *Chem.-Eur. J.*, 2013, **19**, 15378-15383.
127. M. E. Phelps, *Proc. Natl. Acad. Sci. U. S. A.*, 2000, **97**, 9226-9233.
128. K. Stockhofe, J. M. Postema, H. Schieferstein and T. L. Ross, *Pharmaceuticals*, 2014, **7**, 392-418.
129. S. M. Ametamey, M. Honer and P. A. Schubiger, *Chem. Rev.*, 2008, **108**, 1501-1516.
130. S. S. Gambhir, *Nat. Rev. Cancer*, 2002, **2**, 683-693.
131. H. Hong, Y. Zhang, J. Sun and W. Cai, *Nano Today*, 2009, **4**, 399-413.
132. S. B. Lee, H. L. Kim, H. J. Jeong, S. T. Lim, M. H. Sohn and D. W. Kim, *Angew. Chem., Int. Ed.*, 2013, **52**, 10549-10552.
133. F. Chen, H. Hong, Y. Zhang, H. F. Valdovinos, S. Shi, G. S. Kwon, C. P. Theuer, T. E. Barnhart and W. Cai, *ACS Nano*, 2013, **7**, 9027-9039.
134. L. Miller, G. Winter, B. Baur, B. Witulla, C. Solbach, S. Reske and M. Lindén, *Nanoscale*, 2014, **6**, 4928-4935.
135. R. Kumar, I. Roy, T. Y. Ohulchanskky, L. A. Vathy, E. J. Bergey, M. Sajjad and P. N. Prasad, *ACS Nano*, 2010, **4**, 699-708.
136. X. Huang, F. Zhang, S. Lee, M. Swierczewska, D. O. Kiesewetter, L. Lang, G. Zhang, L. Zhu, H. Gao, H. S. Choi, G. Niu and X. Chen, *Biomaterials*, 2012, **33**, 4370-4378.
137. D. W. Kim, D. S. Ahn, Y. H. Oh, S. Lee, H. S. Kil, S. J. Oh, S. J. Lee, J. S. Kim, J. S. Ryu, D. H. Moon and D. Y. Chi, *J. Am. Chem. Soc.*, 2006, **128**, 16394-16397.
138. P. W. Miller, N. J. Long, R. Vilar and A. D. Gee, *Angew. Chem., Int. Ed.*, 2008, **47**, 8998-9033.
139. R. Schirrmacher, C. Wängler and E. Schirrmacher, *Mini-Rev. Org. Chem.*, 2007, **4**, 317-329.

140. L. S. Rosen, H. I. Hurwitz, M. K. Wong, J. Goldman, D. S. Mendelson, W. D. Figg, S. Spencer, B. J. Adams, D. Alvarez, B. K. Seon, C. P. Theuer, B. R. Leigh and M. S. Gordon, *Clinical Cancer Research*, 2012, **18**, 4820-4829.
141. R. B. Greenwald, H. Zhao, P. Peng, C. B. Longley, Q. H. Dai, J. Xia and A. Martinez, *Eur. J. Med. Chem.*, 2005, **40**, 798-804.
142. W. R. Hendee and E. R. Ritenour, *Medical Imaging Physics*, Wiley-Liss, Inc., New York, 2002.
143. K. Nieman, M. Oudkerk, B. J. Rensing, P. Van Ooijen, A. Munne, R. J. Van Geuns and P. J. De Feyter, *Lancet*, 2001, **357**, 599-603.
144. M. Tepel, P. Aspelin and N. Lameire, *Circulation*, 2006, **113**, 1799-1806.
145. J. Singh and A. Daftary, *Journal of Nuclear Medicine Technology*, 2008, **36**, 69-74.
146. C. Haller and I. Hizoh, *Investigative Radiology*, 2004, **39**, 149-154.
147. F. Alexis, E. Pridgen, L. K. Molnar and O. C. Farokhzad, *Mol. Pharm.*, 2008, **5**, 505-515.
148. X. He, H. Nie, K. Wang, W. Tan, X. Wu and P. Zhang, *Anal. Chem.*, 2008, **80**, 9597-9603.
149. D. P. Cormode and Z. A. Fayad, *Imaging in Medicine*, 2011, **3**, 263-266.
150. N. Lee, S. H. Choi and T. Hyeon, *Adv. Mater. (Weinheim, Ger.)*, 2013, **25**, 2641-2660.
151. Y. Liu, K. Ai and L. Lu, *Acc. Chem. Res.*, 2012, **45**, 1817-1827.
152. H. Lusic and M. W. Grinstaff, *Chem. Rev.*, 2013, **113**, 1641-1666.
153. A. Galperin, D. Margel, J. Baniel, G. Dank, H. Biton and S. Margel, *Biomaterials*, 2007, **28**, 4461-4468.
154. F. Hyafil, J. C. Cornily, J. E. Feig, R. Gordon, E. Vucic, V. Amirbekian, E. A. Fisher, V. Fuster, L. J. Feldman and Z. A. Fayad, *Nat. Med. (N. Y., NY, U. S.)*, 2007, **13**, 636-641.
155. D. Kim, S. Park, H. L. Jae, Y. J. Yong and S. Jon, *J. Am. Chem. Soc.*, 2007, **129**, 7661-7665.
156. C. Kojima, Y. Umeda, M. Ogawa, A. Harada, Y. Magata and K. Kono, *Nanotechnology*, 2010, **21**, 245104.
157. R. Popovtzer, A. Agrawal, N. A. Kotov, A. Popovtzer, J. Balter, T. E. Carey and R. Kopelman, *Nano Lett.*, 2008, **8**, 4593-4596.
158. I. C. Sun, D. K. Eun, J. H. Na, S. Lee, I. I. J. Kim, I. C. Youn, C. Y. Ko, H. S. Kim, D. Lim, K. Choi, P. B. Messersmith, T. G. Park, S. Y. Kim, I. C. Kwon, K. Kim and C. H. Ahn, *Chem.-Eur. J.*, 2009, **15**, 13341-13347+13276.
159. P. A. Jackson, W. N. W. A. Rahman, C. J. Wong, T. Ackerly and M. Geso, *European Journal of Radiology*, 2010, **75**, 104-109.
160. E. E. Connor, J. Mwamuka, A. Gole, C. J. Murphy and M. D. Wyatt, *Small*, 2005, **1**, 325-327.
161. P. Ghosh, G. Han, M. De, C. K. Kim and V. M. Rotello, *Adv. Drug Delivery Rev.*, 2008, **60**, 1307-1315.
162. P. Huang, L. Bao, C. Zhang, J. Lin, T. Luo, D. Yang, M. He, Z. Li, G. Gao, B. Gao, S. Fu and D. Cui, *Biomaterials*, 2011, **32**, 9796-9809.
163. T. Luo, P. Huang, G. Gao, G. Shen, S. Fu, D. Cui, C. Zhou and Q. Ren, *Optics Express*, 2011, **19**, 17030-17039.
164. M. M. Van Schooneveld, D. P. Cormode, R. Koole, J. T. Van Wijngaarden, C. Calcagno, T. Skajaa, J. Hilhorst, D. C. T Hart, Z. A. Fayad, W. J. M. Mulder and A. Meijerink, *Contrast Media and Molecular Imaging*, 2010, **5**, 231-236.
165. O. Rabin, J. M. Perez, J. Grimm, G. Wojtkiewicz and R. Weissleder, *Nat. Mater.*, 2006, **5**, 118-122.
166. Y. Liu, K. Ai, J. Liu, Q. Yuan, Y. He and L. Lu, *Angew. Chem., Int. Ed.*, 2012, **51**, 1437-1442.
167. Z. Liu, Z. Li, J. Liu, S. Gu, Q. Yuan, J. Ren and X. Qu, *Biomaterials*, 2012, **33**, 6748-6757.
168. J. S. Kim, T. J. Yoon, K. N. Yu, B. G. Kim, S. J. Park, H. W. Kim, K. H. Lee, S. B. Park, J. K. Lee and M. H. Cho, *Toxicol. Sci.*, 2006, **89**, 338-347.
169. Y. Liu, K. Ai, J. Liu, Q. Yuan, Y. He and L. Lu, *Advanced Healthcare Materials*, 2012, **1**, 461-466.
170. J. Ma, P. Huang, M. He, L. Pan, Z. Zhou, L. Feng, G. Gao and D. Cui, *J. Phys. Chem. B*, 2012, **116**, 14062-14070.
171. A. Xia, M. Chen, Y. Gao, D. Wu, W. Feng and F. Li, *Biomaterials*, 2012, **33**, 5394-5405.
172. H. Xing, W. Bu, S. Zhang, X. Zheng, M. Li, F. Chen, Q. He, L. Zhou, W. Peng, Y. Hua and J. Shi, *Biomaterials*, 2012, **33**, 1079-1089.
173. G. Zhang, Y. Liu, Q. Yuan, C. Zong, J. Liu and L. Lu, *Nanoscale*, 2011, **3**, 4365-4371.
174. H. D. Liang and M. J. K. Blomley, *British Journal of Radiology*, 2003, **76**, S140-S150.
175. J. U. Voigt, *Methods*, 2009, **48**, 92-97.
176. E. G. Schutt, D. H. Klein, R. M. Mattrey and J. G. Riess, *Angew. Chem., Int. Ed.*, 2003, **42**, 3218-3235.
177. P. A. Dayton and K. W. Ferrara, *Journal of Magnetic Resonance Imaging*, 2002, **16**, 362-377.
178. F. Kiessling, J. Bzyl, S. Fokong, M. Siepmann, G. Schmitz and M. Palmowski, *Curr. Pharm. Des.*, 2012, **18**, 2184-2199.
179. R. Basude, J. W. Duckworth and M. A. Wheatley, *Ultrasound in Medicine and Biology*, 2000, **26**, 621-628.
180. S. Hernot and A. L. Klibanov, *Adv. Drug Delivery Rev.*, 2008, **60**, 1153-1166.
181. E. C. Unger, T. Porter, W. Culp, R. Labell, T. Matsunaga and R. Zutshi, *Adv. Drug Delivery Rev.*, 2004, **56**, 1291-1314.
182. R. Díaz-López, N. Tsapis, M. Santin, S. L. Bridal, V. Nicolas, D. Jaillard, D. Libong, P. Chaminade, V. Marsaud, C. Vauthier and E. Fattal, *Biomaterials*, 2010, **31**, 1723-1731.
183. D. M. El-Sherif and M. A. Wheatley, *Journal of Biomedical Materials Research - Part A*, 2003, **66**, 347-355.
184. B. A. Kaufmann and J. R. Lindner, *Curr. Opin. Biotechnol.*, 2007, **18**, 11-16.
185. S. Casciaro, F. Conversano, A. Ragusa, M. A. Malvindi, R. Franchini, A. Greco, T. Pellegrino and G. Gigli, *Investigative Radiology*, 2010, **45**, 715-724.
186. J. Liu, A. L. Levine, J. S. Mattoon, M. Yamaguchi, R. J. Lee, X. Pan and T. J. Rosol, *Physics in Medicine and Biology*, 2006, **51**, 2179-2189.
187. P. L. Lin, R. J. Eckersley and E. A. H. Hall, *Adv. Mater. (Weinheim, Ger.)*, 2009, **21**, 3949-3952.

188. H. P. Martinez, Y. Kono, S. L. Blair, S. Sandoval, J. Wang-Rodriguez, R. F. Mattrey, A. C. Kummel and W. C. Trogler, *MedChemComm*, 2010, **1**, 266-270.
189. A. Liberman, H. P. Martinez, C. N. Ta, C. V. Barback, R. F. Mattrey, Y. Kono, S. L. Blair, W. C. Trogler, A. C. Kummel and Z. Wu, *Biomaterials*, 2012, **33**, 5124-5129.
190. A. Milgroom, M. Intrator, K. Madhavan, L. Mazzaro, R. Shandas, B. Liu and D. Park, *Colloids and Surfaces B: Biointerfaces*, 2014, **116**, 652-657.
191. H. Hu, H. Zhou, J. Du, Z. Wang, L. An, H. Yang, F. Li, H. Wu and S. Yang, *J. Mater. Chem.*, 2011, **21**, 6576-6583.
192. H. Hu, H. Zhou, J. Liang, L. An, A. Dai, X. Li, H. Yang, S. Yang and H. Wu, *J. Colloid Interface Sci.*, 2011, **358**, 392-398.
193. Y. Chen, Q. Yin, X. Ji, S. Zhang, H. Chen, Y. Zheng, Y. Sun, H. Qu, Z. Wang, Y. Li, X. Wang, K. Zhang, L. Zhang and J. Shi, *Biomaterials*, 2012, **33**, 7126-7137.
194. M. A. Malvindi, A. Greco, F. Conversano, A. Figuerola, M. Corti, M. Bonora, A. Lascialfari, H. A. Doumari, M. Moscardini, R. Cingolani, G. Gigli, S. Casciaro, T. Pellegrino and A. Ragusa, *Adv. Funct. Mater.*, 2011, **21**, 2548-2555.
195. J. Cheon and J. H. Lee, *Acc. Chem. Res.*, 2008, **41**, 1630-1640.
196. J. Kim, Y. Piao and T. Hyeon, *Chem. Soc. Rev.*, 2009, **38**, 372-390.
197. J. Liao, T. Qi, B. Chu, J. Peng, F. Luo and Z. Qian, *J. Nanosci. Nanotechnol.*, 2014, **14**, 175-189.
198. M. Mahmoudi, V. Serpooshan and S. Laurent, *Nanoscale*, 2011, **3**, 3007-3029.
199. J. M. Rosenholm, C. Sahlgren and M. Lindén, *Curr. Drug Targets*, 2011, **12**, 1166-1186.
200. M. Swierczewska, S. Lee and X. Chen, *Mol. Imaging*, 2011, **10**, 3-16.
201. P. Tallury, K. Payton and S. Santra, *Nanomedicine*, 2008, **3**, 579-592.
202. X. Li, D. Zhao and F. Zhang, *Theranostics*, 2013, **3**, 292-305.
203. Q. Xiao, X. Zheng, W. Bu, W. Ge, S. Zhang, F. Chen, H. Xing, Q. Ren, W. Fan, K. Zhao, Y. Hua and J. Shi, *J. Am. Chem. Soc.*, 2013, **135**, 13041-13048.
204. M. Liong, J. Lu, M. Kovochich, T. Xia, S. G. Ruehm, A. E. Nel, F. Tamanoi and J. I. Zink, *ACS Nano*, 2008, **2**, 889-896.
205. J. E. Lee, N. Lee, H. Kim, J. Kim, S. H. Choi, J. H. Kim, T. Kim, I. C. Song, S. P. Park, W. K. Moon and T. Hyeon, *J. Am. Chem. Soc.*, 2010, **132**, 552-557.
206. J. Liu, J. Bu, W. Bu, S. Zhang, L. Pan, W. Fan, F. Chen, L. Zhou, W. Peng, K. Zhao, J. Du and J. Shi, *Angew. Chem., Int. Ed.*, 2014, **53**, 4551-4555.
207. F. Chen, H. Hong, S. Shi, S. Goel, H. F. Valdovinos, R. Hernandez, C. P. Theuer, T. E. Barnhart and W. Cai, *Scientific Reports*, 2014, **4**.
208. F. Wang, X. Chen, Z. Zhao, S. Tang, X. Huang, C. Lin, C. Cai and N. Zheng, *J. Mater. Chem.*, 2011, **21**, 11244-11252.
209. E. Lipani, S. Laurent, M. Surin, L. Vander Elst, P. Lecleìre and R. N. Muller, *Langmuir*, 2013, **29**, 3419-3427.
210. Z. Zheng, A. Daniel, W. Yu, B. Weber, J. Ling and A. H. E. Müller, *Chem. Mater.*, 2013, **25**, 4585-4594.
211. X. Hu, M. Wang, F. Miao, J. Ma, H. Shen and N. Jia, *Journal of Materials Chemistry B*, 2014, **2**, 2265-2275.
212. S. Sahu, N. Sinha, S. K. Bhutia, M. Majhi and S. Mohapatra, *Journal of Materials Chemistry B*, 2014, **2**, 3799-3808.
213. E. S. Jang, S. Y. Lee, E. J. Cha, I. C. Sun, I. C. Kwon, D. Kim, Y. I. Kim, K. Kim and C. H. Ahn, *Pharm. Res.*, 2014.
214. S. Chen, Y. Yang, H. Li, X. Zhou and M. Liu, *Chem. Commun.*, 2014, **50**, 283-285.
215. H. L. Liu, M. Y. Hua, H. W. Yang, C. Y. Huang, P. N. Chu, J. S. Wu, I. C. Tseng, J. J. Wang, T. C. Yen, P. Y. Chen and K. C. Wei, *Proc. Natl. Acad. Sci. U. S. A.*, 2010, **107**, 15205-15210.
216. A. Louie, *Chem. Rev.*, 2010, **110**, 3146-3195.
217. D. Vlaskou, O. Mykhaylyk, F. Krötz, N. Hellwig, R. Renner, U. Schillinger, B. Gleich, A. Heidsieck, G. Schmitz, K. Hensel and C. Plank, *Adv. Funct. Mater.*, 2010, **20**, 3881-3894.
218. F. Yang, Y. Li, Z. Chen, Y. Zhang, J. Wu and N. Gu, *Biomaterials*, 2009, **30**, 3882-3890.
219. Y. Chen, H. Chen, Y. Sun, Y. Zheng, D. Zeng, F. Li, S. Zhang, X. Wang, K. Zhang, M. Ma, Q. He, L. Zhang and J. Shi, *Angew. Chem., Int. Ed.*, 2011, **50**, 12505-12509.
220. L. An, H. Hu, J. Du, J. Wei, L. Wang, H. Yang, D. Wu, H. Shi, F. Li and S. Yang, *Biomaterials*, 2014, **35**, 5381-5392.
221. W. Cai, K. Chen, Z. B. Li, S. S. Gambhir and X. Chen, *Journal of Nuclear Medicine*, 2007, **48**, 1862-1870.
222. K. Chen, Z. B. Li, H. Wang, W. Cai and X. Chen, *European Journal of Nuclear Medicine and Molecular Imaging*, 2008, **35**, 2235-2244.
223. Y. Sun, M. Yu, S. Liang, Y. Zhang, C. Li, T. Mou, W. Yang, X. Zhang, B. Li, C. Huang and F. Li, *Biomaterials*, 2011, **32**, 2999-3007.
224. L. Tang, X. Yang, L. W. Dobrucki, I. Chaudhury, Q. Yin, C. Yao, S. Lezmi, W. G. Helferich, T. M. Fan and J. Cheng, *Angew. Chem., Int. Ed.*, 2012, **51**, 12721-12726.
225. M. S. Bradbury, E. Phillips, P. H. Montero, S. M. Cheal, H. Stambuk, J. C. Durack, C. T. Sofocleous, R. J. C. Meester, U. Wiesner and S. Patel, *Integrative Biology (United Kingdom)*, 2013, **5**, 74-86.
226. A. A. Burns, J. Vider, H. Ow, E. Here, P. M. Oula, M. Baumgart, S. M. Larson, U. Wiesner and M. Bradbury, *Nano Lett.*, 2009, **9**, 442-448.
227. F. Chen, T. R. Nayak, S. Goel, H. F. Valdovinos, H. Hong, C. P. Theuer, T. E. Barnhart and W. Cai, *Mol. Pharm.*, 2014.
228. K. Hayashi, M. Nakamura, H. Miki, S. Ozaki, M. Abe, T. Matsumoto and K. Ishimura, *Chem. Commun.*, 2013, **49**, 5334-5336.
229. K. Hayashi, M. Nakamura and K. Ishimura, *Advanced Healthcare Materials*, 2013, **2**, 756-763.
230. F. Liu, X. He, L. Liu, H. You, H. Zhang and Z. Wang, *Biomaterials*, 2013, **34**, 5218-5225.
231. C. Y. Ang, S. Y. Tan and Y. Zhao, *Organic and Biomolecular Chemistry*, 2014, **12**, 4776-4806.
232. R. Bardhan, S. Lal, A. Joshi and N. J. Halas, *Acc. Chem. Res.*, 2011, **44**, 936-946.
233. V. Biju, *Chem. Soc. Rev.*, 2014, **43**, 744-764.
234. I. Brigger, C. Dubernet and P. Couvreur, *Adv. Drug Delivery Rev.*, 2002, **54**, 631-651.
235. N. T. Chen, S. H. Cheng, J. S. Souris, C. T. Chen, C. Y. Mou and L. W. Lo, *Journal of Materials Chemistry B*, 2013, **1**, 3128-3135.

236. M. L. Etheridge, S. A. Campbell, A. G. Erdman, C. L. Haynes, S. M. Wolf and J. McCullough, *Nanomedicine: Nanotechnology, Biology, and Medicine*, 2013, **9**, 1-14.
237. C. S. Kim, G. Y. Tonga, D. Solfiell and V. M. Rotello, *Adv. Drug Delivery Rev.*, 2013, **65**, 93-99.
238. Z. Li, J. C. Barnes, A. Bosoy, J. F. Stoddart and J. I. Zink, *Chem. Soc. Rev.*, 2012, **41**, 2590-2605.
239. V. Mamaeva, C. Sahlgren and M. Lindén, *Adv. Drug Delivery Rev.*, 2013, **65**, 689-702.
240. S. Nazir, T. Hussain, A. Ayub, U. Rashid and A. J. MacRobert, *Nanomedicine: Nanotechnology, Biology, and Medicine*, 2014, **10**, 19-34.
241. C. Nilsson, B. Barrios-Lopez, A. Kallinen, P. Laurinmäki, S. J. Butcher, M. Raki, J. Weisell, K. Bergström, S. W. Larsen, J. Østergaard, C. Larsen, A. Urtti, A. J. Airaksinen and A. Yaghmur, *Biomaterials*, 2013, **34**, 8491-8503.
242. Q. Zhang, X. Wang, P. Z. Li, K. T. Nguyen, X. J. Wang, Z. Luo, H. Zhang, N. S. Tan and Y. Zhao, *Adv. Funct. Mater.*, 2014, **24**, 2450-2461.
243. M. Colilla, B. González and M. Vallet-Regí, *Biomaterials Science*, 2013, **1**, 114-134.
244. S. Mura, J. Nicolas and P. Couvreur, *Nat. Mater.*, 2013, **12**, 991-1003.
245. J. L. Vivero-Escoto and D. L. Vega, *RSC Advances*, 2014, **4**, 14400-14407.
246. L. Du, S. Liao, H. A. Khatib, J. F. Stoddart and J. I. Zink, *J. Am. Chem. Soc.*, 2009, **131**, 15136-15142.
247. X. Hu, Y. Wang and B. Peng, *Chemistry - An Asian Journal*, 2014, **9**, 319-327.
248. R. Liu, Y. Zhang, X. Zhao, A. Agarwal, L. J. Mueller and P. Feng, *J. Am. Chem. Soc.*, 2010, **132**, 1500-1501.
249. J. T. Sun, C. Y. Hong and C. Y. Pan, *J. Phys. Chem. C*, 2010, **114**, 12481-12486.
250. A. Agostini, L. Mondragón, C. Coll, E. Aznar, M. D. Marcos, R. Martínez-Máñez, F. Sancenón, J. Soto, E. Pérez-Payá and P. Amorós, *ChemistryOpen*, 2012, **1**, 17-20.
251. Y. L. Sun, Y. Zhou, Q. L. Li and Y. W. Yang, *Chem. Commun.*, 2013, **49**, 9033-9035.
252. R. Liu, X. Zhao, T. Wu and P. Feng, *J. Am. Chem. Soc.*, 2008, **130**, 14418-14419.
253. A. Baeza, E. Guisasola, E. Ruiz-Hernández and M. Vallet-Regí, *Chem. Mater.*, 2012, **24**, 517-524.
254. E. Ruiz-Hernández, A. Baeza and M. Vallet-Regí, *ACS Nano*, 2011, **5**, 1259-1266.
255. J. Croissant and J. I. Zink, *J. Am. Chem. Soc.*, 2012, **134**, 7628-7631.
256. D. P. Ferris, Y. L. Zhao, N. M. Khashab, H. A. Khatib, J. F. Stoddart and J. I. Zink, *J. Am. Chem. Soc.*, 2009, **131**, 1686-1688.
257. H. Li, L. L. Tan, P. Jia, Q. L. Li, Y. L. Sun, J. Zhang, Y. Q. Ning, J. Yu and Y. W. Yang, *Chemical Science*, 2014, **5**, 2804-2808.
258. C. R. Thomas, D. P. Ferris, J. H. Lee, E. Choi, M. H. Cho, E. S. Kim, J. F. Stoddart, J. S. Shin, J. Cheon and J. I. Zink, *J. Am. Chem. Soc.*, 2010, **132**, 10623-10625.
259. D. Tarn, D. P. Ferris, J. C. Barnes, M. W. Ambrogio, J. F. Stoddart and J. I. Zink, *Nanoscale*, 2014, **6**, 3335-3343.
260. Y. Chen, H. Chen and J. Shi, *Expert Opinion on Drug Delivery*, 2014, **11**, 917-930.
261. J. Funkhouser, *Current Drug Discovery*, 2002, **2**, 17-19.
262. Z. Tao, *RSC Advances*, 2014, **4**, 18961-18980.
263. M. Xie, H. Shi, Z. Li, H. Shen, K. Ma, B. Li, S. Shen and Y. Jin, *Colloids and Surfaces B: Biointerfaces*, 2013, **110**, 138-147.
264. J. Wang, P. P. Gao, X. X. Yang, T. T. Wang, J. Wang and C. Z. Huang, *Journal of Materials Chemistry B*, 2014, **2**, 4379-4386.
265. Q. Xing, N. Li, D. Chen, W. Sha, Y. Jiao, X. Qi, Q. Xu and J. Lu, *Journal of Materials Chemistry B*, 2014, **2**, 1182-1189.
266. J. H. Park, L. Gu, G. Von Maltzahn, E. Ruoslahti, S. N. Bhatia and M. J. Sailor, *Nat. Mater.*, 2009, **8**, 331-336.
267. H. Chen, Z. Zhen, W. Tang, T. Todd, Y. J. Chuang, L. Wang, Z. Pan and J. Xie, *Theranostics*, 2013, **3**, 650-657.
268. H. Chen, D. Sulejmanovic, T. Moore, D. C. Colvin, B. Qi, O. T. Mefford, J. C. Gore, F. Alexis, S. J. Hwu and J. N. Anker, *Chem. Mater.*, 2014, **26**, 2105-2112.
269. Y. Chen, H. Chen, S. Zhang, F. Chen, S. Sun, Q. He, M. Ma, X. Wang, H. Wu, L. Zhang, L. Zhang and J. Shi, *Biomaterials*, 2012, **33**, 2388-2398.
270. M. Wu, Q. Meng, Y. Chen, P. Xu, S. Zhang, Y. Li, L. Zhang, M. Wang, H. Yao and J. Shi, *Adv. Funct. Mater.*, 2014.
271. W. Fan, B. Shen, W. Bu, F. Chen, K. Zhao, S. Zhang, L. Zhou, W. Peng, Q. Xiao, H. Xing, J. Liu, D. Ni, Q. He and J. Shi, *J. Am. Chem. Soc.*, 2013, **135**, 6494-6503.
272. M. Ma, H. Chen, Y. Chen, X. Wang, F. Chen, X. Cui and J. Shi, *Biomaterials*, 2012, **33**, 989-998.
273. S. H. Seo, B. M. Kim, A. Joe, H. W. Han, X. Chen, Z. Cheng and E. S. Jang, *Biomaterials*, 2014, **35**, 3309-3318.
274. S. Shen, H. Tang, X. Zhang, J. Ren, Z. Pang, D. Wang, H. Gao, Y. Qian, X. Jiang and W. Yang, *Biomaterials*, 2013, **34**, 3150-3158.
275. H. X. Xia, X. Q. Yang, J. T. Song, J. Chen, M. Z. Zhang, D. M. Yan, L. Zhang, M. Y. Qin, L. Y. Bai, Y. D. Zhao and Z. Y. Ma, *Journal of Materials Chemistry B*, 2014, **2**, 1945-1953.
276. B. Xu, Y. Ju, Y. Cui, G. Song, Y. Iwase, A. Hosoi and Y. Morita, *Langmuir*, 2014, **30**, 7789-7797.
277. Z. Zhang, L. Wang, J. Wang, X. Jiang, X. Li, Z. Hu, Y. Ji, X. Wu and C. Chen, *Adv. Mater. (Weinheim, Ger.)*, 2012, **24**, 1418-1423.